Luminosity Measurement at the Compact Linear Collider

Rina Schwartz[1]

December 17, 2012

[1]The research work for this thesis was carried out in the Experimental High Energy Physics Group of the Tel Aviv University under the supervision of Prof. **Halina Abramowicz** and Prof. **Aharon Levy**.

Abstract

The compact linear collider (CLIC) is a proposed high energy accelerator, planned to collide electrons with positrons at a maximal center-of-mass energy of 3 TeV, and a peak luminosity of $5.9 \cdot 10^{34}\,\mathrm{cm}^{-2}\mathrm{s}^{-1}$. Complementary to the large hadron collider, CLIC is to provide high precision measurements of both known and new physics processes.

The required relative precision of luminosity measurement at the CLIC is 10^{-2}. The measurement will be done by the luminosity calorimeter (LumiCal), designed to measure the rate of low angles Bhabha scattering events, a process with well-known cross-section from electroweak theory. Beam-beam effects, which are of unprecedented intensity at the CLIC, influence the luminosity spectrum shape and create a significat amount of background charge deposits in the LumiCal, thus setting a challenge on the requirement for precision. The ability of the LumiCal to provide accurate luminosity measurement depends on its ability to perform accurate energy reconstruction of Bhabha events.

In this work, the issue of in-situ calibration of the LumiCal is addressed for the first time. Using a wide range of software tools, the foreseen luminosity spectrum is fully simulated and reconstructed, and a process of calibration is established and proven to be feasible with adequate accuracy.

In addition, the issue of energy resolution of the LumiCal is re-examined within the full detector simulation, and in the presence of beam-induced background, with implications on time-stamping of the readout electronics.

Contents

Chapter 1

Introduction

1.1 The Compact Linear Collider

1.1.1 Physics Potential of the CLIC

Elementary particle physics has always progressed by attacking its mysteries simultaneously from many different directions. As particle physics has moved to increasing high energy, the facilities needed to reach these energies have become progressively more expensive, which implies that experimental efforts must be consolidated into the most promising channels. The exploration of the 100 GeV mass scale has been carried out by proton-antiproton experiments at CERN and Fermilab, electron-positron annihilation experiments at SLAC and CERN, and electron-proton scattering experiments at DESY; all of these experiments have contributed pieces to the major result, the precise confirmation of the standard model for electroweak and strong interactions. Following reference [1], a crucial problem to be solved by the next generation of accelerators is to find the mechanism for the spontaneous breaking of the electroweak gauge symmetry.

Currently, the large hadron collider (LHC) is running successfully, colliding proton beams at centre-of-mass (c.m.s.) energy of 8 TeV. The c.m.s. energy is planned to be increased to a maximal value of 14 TeV. The LHC will allow unprecedented exploration of the mechanism of electroweak symmetry breaking and of the physical phenomena at the TeV scale. It is quite likely that the discoveries made at the LHC will alter the present views of the particle world. The compact linear collider (CLIC) is a proposed high energy accelerator, planned to collide electrons with positrons at a maximal

c.m.s. energy of 3 TeV. The present knowledge of the Standard Model (SM) and the many experimental constraints on new theories allow physicists to envision plausible scenarios for which the CLIC will be necessary in pushing forward research in particle physics, beyond the results that will be reached by the LHC. CLIC holds physics capabilities in the following categories [2]: Higgs physics, supersymmetry, strongly interacting electroweak theories, and precision physics.

The Higgs boson, the particle responsible for the electroweak symmetry breaking in the standard model, was the most plausible anticipated discovery at the LHC until recently, when a signal of a boson compatible with the Higgs boson was found at about 125 GeV both by the CMS [3] and the Atlas [4] experiments. The LHC can only partially answer all questions regarding its true nature, such as: is it a fundamental particle or a composite one? Is it part of a more complicated electroweak sector? Does it universally couple to all matter proportionally to mass? CLIC can explore these issues in much greater depth and unravel these questions by measuring the Higgs couplings to an unprecedented precision.

Supersymmetry is often considered an attractive option to deal with the naturalness problem of the Higgs boson [2]. If supersymmetry indeed lies near the weak scale, the LHC is bound to discover it. Heavy sleptons, neutralinos and charginos can only be produced copiously at the LHC through decay chains of strongly-interacting supersymmetric particles and, in some cases, these chains do not access all states. On the other hand, CLIC can explore thoroughly the TeV region, looking for any new particles with electroweak charges.

A fundamental question in particle physics concerns the origin of dark matter. The precise mass and coupling measurements that can be performed at CLIC are crucial to address fundamental questions about the mechanism of supersymmetry breaking, about certain aspects of unification theories, and about the viability of the lightest supersymmetric particle as a dark matter thermal relic.

To conclude, the extended discovery reach and the enhanced precision measurements provided by CLIC are likely to be the necessary tools to address many of the fundamental questions about the weak scale left unanswered by the LHC. Quantitative improvement in a measurement may lead to a qualitative jump in the understanding of the underlying physics, and the accuracy that can be reached at CLIC is likely to open new avenues in our understanding of the particle world.

1.1.2 Design of the CLIC

The next e^+e^- linear collider aims to fulfill the requirement of high luminosity at the TeV region. In the past two decades several linear collider models have been studied [5, 6, 7], and in 2004 efforts were joined for a study of the proposed international linear collider (ILC) [8]. The overall system design of the ILC has been chosen to realize the physics requirements with a maximum c.m.s. energy of 500 GeV and a peak luminosity of $2{\cdot}10^{34}\,\mathrm{cm}^{-2}\mathrm{s}^{-1}$. The ILC is designed to be 31 km in total length, and in case of machine upgrade to 1 TeV would be extended by ~ 22 km. The CLIC is a proposed linear collider with one distinct advantage over the ILC in the accelerating mechanism, resulting in a higher c.m.s. energy, as discussed below. The total length of the CLIC is planned to be 48.1 km as indicated in Fig. 1.1, where a schematic design of the CLIC is depicted.

In order to reach high energies with a linear collider, a cost-effective technology is of prime importance. Instead of klystrons-generated RF power used to accelerate the main beams in conventional linear accelerators, the CLIC concept is based on the two-beam accelerator scheme. The RF power is extracted from a low-energy, high-current, drive beam which is decelerated in power extraction and transfer structures of low impedance. This power is then directly transferred into the high-impedance structures of the main linac and used to accelerate the high-energy, low-current main beam, which is later brought into collision. The two-beam approach to acceleration offers a solution that avoids the use of a large number of active RF elements in the main linac.

In principle, a first CLIC stage could cover c.m.s. energies between $\sim$0.1 and 0.5 TeV with a luminosity of $\mathcal{L} = 10^{33} - 10^{34}\,\mathrm{cm}^{-2}\,\mathrm{s}^{-1}$, providing an interesting physics overlap with the LHC. This stage could then be extended first to 1 TeV, with $\mathcal{L}$ above $10^{34}\,\mathrm{cm}^{-2}\,\mathrm{s}^{-1}$, and then to multi-TeV operation, with e^+e^-collisions at 3 TeV and a peak luminosity of $5.9 \cdot 10^{34}\,\mathrm{cm}^{-2}\mathrm{s}^{-1}$, which should break new physics ground. A final stage might reach a collision energy of 5 TeV or more [2].

1.2 The CLIC Detector

The physics program at CLIC places stringent requirements on the detector performance. These include precise momentum resolution, vertex reconstruction, particle identification, excellent jet reconstruction and hermetic cover-

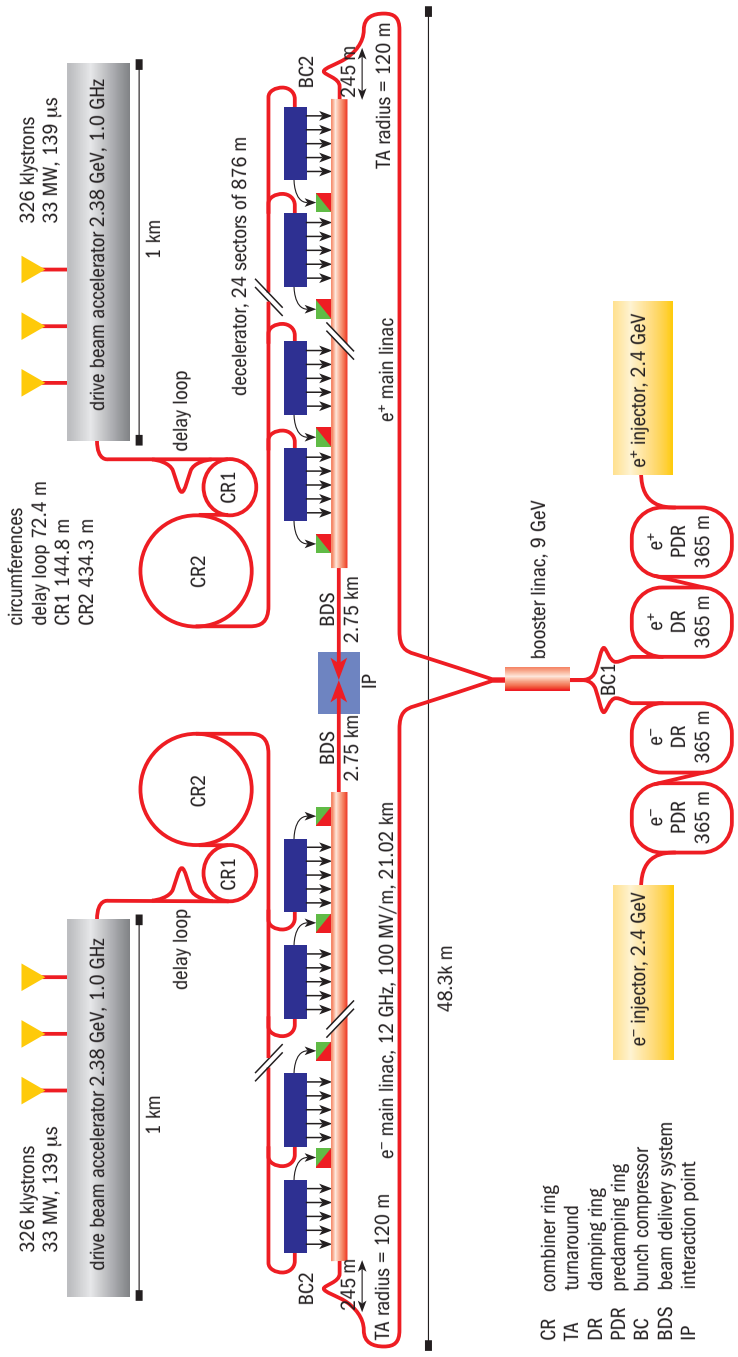

Figure 1.1: Schematic design of the CLIC

age. For the ILC, with similar detector requirements, albeit at a lower energy, two general purpose detector concepts have been developed into mature designs over the last decade. One is the international large detector (ILD), and the other is the silicon detector concept (SiD). Both of these concepts were evaluated and validated by the international detector advisory group (IDAG). These concepts are used as starting points for CLIC detectors, with modifications motivated by the more challenging experimental conditions at CLIC and by the higher collision energy. In particular, the detector must be able to cope with the relatively high levels of background, which in turn dictates the timing and readout requirements for the detector subsystems.

Both detector concepts (ILD and SiD) have a similar general design, with a large solenoid which contains a micro-vertex detector, tracking device and electromagnetic and hadronic highly-granular calorimetry. However, they differ in the detailed approach. The ILD design aims for an optimized jet reconstruction with calorimetry at a relatively large radius and consequently a smaller magnetic field of 4 T, and a large TPC as main tracking detector. The SiD is designed as a compact, cost-optimized detector with a 5 T solenoid and high precision all-silicon tracking. Starting from these two designs, two CLIC detector concepts have been developed [2], referred to as CLIC_ILD and CLIC_SiD, respectively. As for the ILC, CLIC is foreseeing a push-pull mechanism to alternately operate both detectors at a single interaction region. The work presented in this compilation follows the CLIC_ILD model which is depicted in Fig. 1.2.

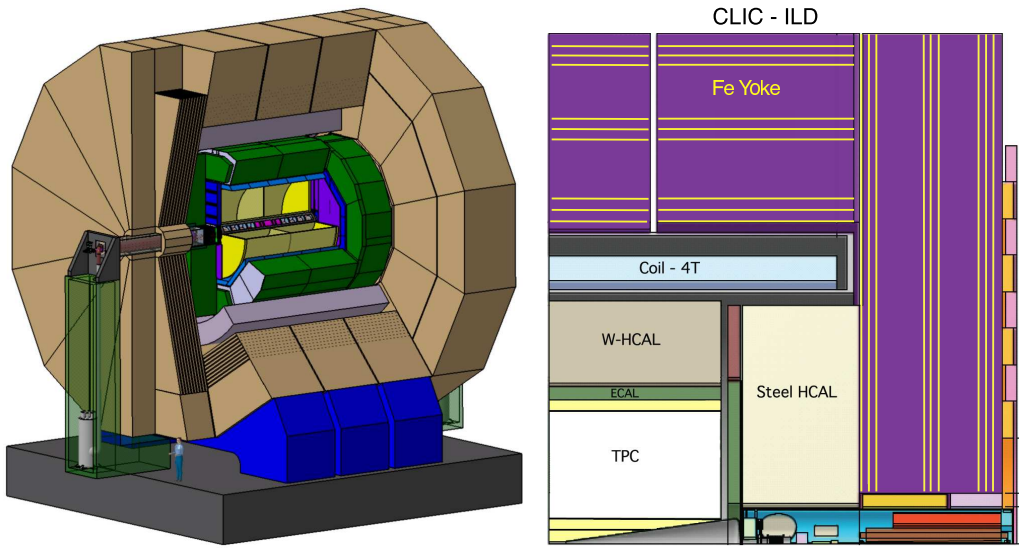

(a) (b)

Figure 1.2: (a) View of the ILD detector concept. (b) Overall layout of the CLIC_ILD detector concept, in longitudinal and transverse cuts. (The figures are taken from [2, 9]).

1.2.1 The Forward Region of the CLIC Detector

Two calorimeters are foreseen in the very forward region of a CLIC detector; the luminosity calorimeter (LumiCal) for the precise measurement of the luminosity; the beam calorimeter (BeamCal) for the fast estimate of the luminosity and tagging of high energy electrons. Both detectors are realized as sampling calorimeters using tungsten as absorber, centred around the outgoing beams. Silicon sensors are employed for LumiCal, while several technologies are an option for radiation-hard BeamCal sensors [10]. The forward region also contains masking to prevent particles produced by the beam-beam interaction from backscattering into the main detectors and to protect the equipment downstream of the BeamCal, such as the beam position monitor (BPM) and a kicker of the intra train feedback, and the final focus quadrupole (QD0). A conceptual drawing of the very forward region of a CLIC_ILD detector is shown in Fig. 1.3.

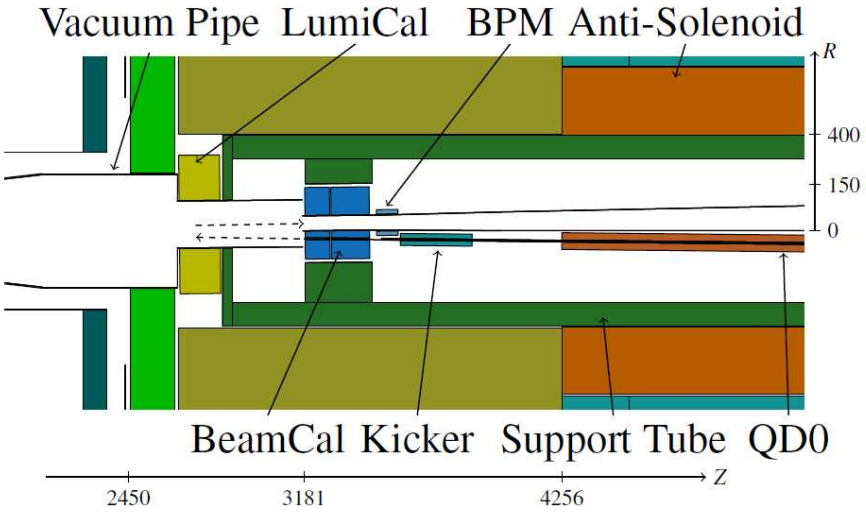

Figure 1.3: Forward region layout of the CLIC_ILD detector concept.

The LumiCal will count precisely the number of Bhabha scattering events in an angular region between roughly 40 and 100 mrad, by reconstructing the electromagnetic shower of the scattered Bhabha particles. It is located behind the electromagnetic calorimeter (ECal) endcap [2], as shown in Fig. 1.3. The role of the ECal is primarily to measure the electron and photon energies individually, as well as the early parts of showers initiated by hadrons. The ECal endcap partially covers the front-face of the LumiCal.

The BeamCal extends the angular coverage of the forward calorimeters, covering the polar angle range between 10 mrad and 40 mrad around the outgoing beam. This calorimeter has three main functions; (1) it serves as shielding for the accelerator components downstream, e.g. the QD0, and as a mask against backscattering into the vertex detector region; (2) it improves the forward hermeticity of the electromagnetic calorimeter system, allowing e.g. to detect low angle high energy electrons from SM processes; (3) it measures a high flux of incoherent pairs, which may be used for luminosity monitoring purposes. All detectors in the very forward region have to tackle relatively high occupancy, requiring special front-end electronics.

The FCAL collaboration has as mission the design and, in the future, the construction of the calorimeters in the forward region of the CLIC (and/or the ILC). The research done by the collaboration comprises optimization of

the design of the very forward region using Monte-Carlo simulations, R&D of radiation-hard solid state sensors and fast front-end readout electronics and performance tests of detectors prototype. FCAL works in collaboration with the detector concepts ILD and SiD of the International Linear Collider and the CLIC detector development group.

During 2011, FCAL contributed to volume 2 of the CLIC conceptual design report (CDR) [2]. The CLIC CDR summarizes the concept of a linear collider based on the CLIC technology, its physics case and the expected performance and design of the physics detectors. It is composed of 3 parts: volume 1 covers the accelerator and technical systems; volume 2 includes physics and detectors studies; volume 3 provides a summary of both technical volumes, as well as input on strategic choices (e.g. energy, luminosity, physics potential) for a future CLIC accelerator.

1.3 Work Scope

The focus of this thesis is the performance of the luminosity calorimeter. In previous studies, the LumiCal design was optimized for both CLIC and ILC c.m.s. energies (see [10, 11], respectively). The question to be answered is whether the current design of the LumiCal allows the precision requirements on the luminosity measurement to be met in the CLIC experimental environment. In order to provide an answer, two contributions to the uncertainty in the measured luminosity are examined; the accuracy in determination of the energy scale, and the energy resolution in the presence of beam induced background.

Many of the interesting physics processes at CLIC are likely to have small cross sections, typically in the few fb range. Therefore, the need for high luminosities is a driving factor in the CLIC accelerator design. One consequence of the small bunch sizes required to achieve high luminosities at CLIC, is the phenomenon of the strong electromagnetic radiation (beamstrahlung) from the electron and positron bunches in the high field of the opposite beam. These beamstrahlung effects, which are largest at the highest c.m.s. energy, have a major impact on the effective luminosity spectrum of the CLIC which has a peak around the beam c.m.s. energy and a long tail towards lower energies. For 3 TeV operation at a total luminosity of $5.9 \cdot 10^{34}\,\mathrm{cm}^{-2}\,\mathrm{s}^{-1}$, the luminosity in the most energetic 1% fraction of the spectrum, defined as the peak luminosity, is $2.0 \cdot 10^{34}\,\mathrm{cm}^{-2}\,\mathrm{s}^{-1}$. The integrated luminosity will be determined directly from a measurement of the rate of Bhabha scattering

events. To match the expected statistical error for measuring electroweak processes in a typical year (500 fb^{-1}) at the CLIC, an accuracy of better than 10^{-2} in the luminosity measurement is needed.

The high energy Bhabha scattering events will be identified based on their energy deposits in the LumiCal, and their acolinearity. The value of the reconstructed energy is obtained by applying calibration constants to the charge collected in the luminosity detector. A pure sample of Bhabha scattering events may be obtained by requiring that the total energy deposited in the LumiCal is greater than 80% of the nominal scattering energy. Because of the selection of Bhabha scattering events which relies on the deposited energy, a shift in the energy scale introduces a bias in the luminosity measurement. It is therefore necessary to accurately determine the LumiCal absolute energy scale. The issue of in-situ energy calibration of the LumiCal will be adressed here for the first time. The energy scale will be determined from the reconstructed shape of the luminosity spectrum. Using generator and detector level Monte-Carlo simulations, it is possible to reconstruct the spectrum and estimate the accuracy in determination of the energy scale and its contribution to the luminosity uncertainty.

The detector readout requirements at the CLIC are closely linked to the beam structure and to the presence of beam-induced background, as well as to the needs for high precision measurements. The interesting high energy e^+e^- events are rare, at most one event per bunch train, however the beam-induced background leads to many additional particles traversing the detectors and to high cell occupancies. The amount of background particles fluctuates on a bunch crossing basis, and the energy they deposit in the detector adds to the Bhabha events signal. A deterioration in the energy resolution is foreseen, depending on the readout time stamping. The precision requirements on the luminosity measurement sets a lower bound to the readout rate. The energy resolution of the LumiCal have been studied previously, for the stand-alone calorimeter [12]. Here, the energy resolution of the LumiCal within the full detector and in presence of beam-induced background is studied.

This work includes a theoretical and experimental introduction (chapter 2), an overview of the LumiCal performance and in-situ energy calibration in the CLIC experimental environment (chapter 3), a study of the beam induced background to the luminosity measurement (chapter 4), an overview of the LumiCal performance in the presence of beam-induced background (chapter 5), and finally, a summary of the results (Table 5.1).

Chapter 2

Luminosity

2.1 Luminosity Measurement at the CLIC

Luminosity is a key quantity to extract the cross section values of all physical processes at a given collider. At CLIC, the integrated luminosity, $\mathcal{L}_{int}$, will be determined from the counting of Bhabha events, N_B, and a theoretical calculation of the Bhabha cross section [2], σ_B,

$$\mathcal{L}_{int} = \frac{N_B}{\sigma_B}, \tag{2.1}$$

where $\mathcal{L}_{int}$ is the luminosity integrated over a data taking period, N_B is the corrected number of Bhabha events detected within a certain acceptance region corresponding to the same period, and σ_B the expected cross section calculated from theory. The ability to calculate the theoretical cross section to high accuracy [13], and an event rate that exceeds by far other physical processes, motivates the use of Bhabha scattering as a gauge process for the luminosity measurement.

There are several effects which may change the c.m.s. energy of the Bhabha scattered particles away from the nominal, e.g. 3 TeV; the beam energy spread (BES) from the main linac, beam-beam interactions, and the initial state radiation. The latter can be calculated with high accuracy and is generally accounted for in event generators such as WHIZARD [14]. BES and beam-beam effects lead to the luminosity spectrum (also referred to as $d\mathcal{L}/d\sqrt{s}$, the differential luminosity). To achieve precise physics results at CLIC, the accurate determination of the luminosity spectrum is a key ingredient.

The luminosity measurement has two components; (1) the luminosity normalization in the high energy peak, using the large cross section for small-angle Bhabha scattering events; (2) the relative shape of the luminosity spectrum, using wide-angle Bhabha events. The small-angle Bhabha events will be measured by the luminosity calorimeter, LumiCal. The calibration of the luminosity spectrum is obtained from LumiCal with its good absolute accuracy. Therefore, LumiCal is a precision device with challenging requirements, e.g. on the mechanical precision and the position control [2].The requirement for LumiCal is to enable a measurement of the integrated luminosity a CLIC with a relative precision smaller than 1% [11].

2.1.1 Bhabha Scattering as a Gauge Process

Bhabha scattering is essentially the process of e^+e^- elastic scattering, via a γ or Z^0 exchange, as depicted in Fig. 2.1.1. Classical electrodynamics dictates

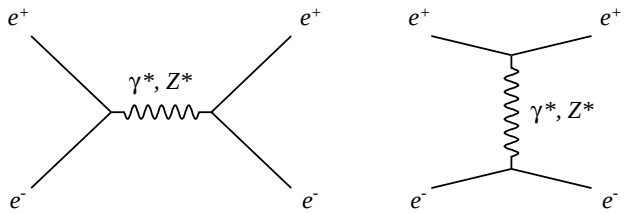

Figure 2.1: Feynman diagrams of the (a) s- and (b) t-channel Born-level elastic Bhabha scattering.

that when scattering, the electron[1] must emit some amount of electromagnetic radiation. So in practice, the final state contains also photons

$$e^+e^- \rightarrow e^+e^-(\gamma). \tag{2.2}$$

One can think of the inclusive Bhabha scattering as a three steps process,

1. emission of radiation from the initial state particles (ISR);
2. elastic Bhabha scattering;
3. emission of radiation from the final state particles (FSR).

[1]Unless otherwise stated "electron" is always meant as "electron or positron"

Due to ISR, the elastic Bhabha scattering in step 2 may be initiated by particles of non-equal four-momenta, and their c.m.s. frame is boosted relative to the lab frame. Generally, the radiation is emitted within a cone whose opening angle shrinks like m/E as the energy increases, where m and E are the electron mass and energy, respectively [13]. At the CLIC, $m/E \simeq 3 \cdot 10^{-7}$; therefore the ISR will proceed within the beampipe, undetected, whereas FSR will leave energy deposit in the detector along with the electron. Moreover, the Bhabha events that will be detected in the LumiCal are those with scattering angles that exceed by far the collinearity cone limit with respect to the incoming lepton momenta.

In leading order, the cross section for electron and positron interaction by exchange of a space-like or a time-like photon, may be presented as the sum of three terms [15],

$$\frac{d\sigma_{\mathrm{B}}}{d\Omega} = \frac{\alpha^2}{2s}\left[\frac{1+\cos^4(\theta/2)}{\sin^4(\theta/2)} - 2\,\frac{\cos^4(\theta/2)}{\sin^2(\theta/2)} + \frac{1+\cos^2\theta}{2}\right], \tag{2.3}$$

where θ is the angle of the scattered lepton with respect to the incoming lepton direction in the c.m.s., α is the electromagnetic fine structure constant, and s is the c.m.s. energy squared. This cross section is calculated under the assumption that the lepton mass is negligible compared to their energy, which is valid at the CLIC c.m.s. energy. The first and last terms correspond to γ exchange in the t- and s-channels, respectively, and the middle term reflects the $s-t$ interference. For very small angles ($\theta \leq 10^\circ$), Bhabha scattering is dominated by the t-channel exchange of a photon [13]. Discounting the s-channel contributions, one can rewrite Eq. (2.3) in terms of the scattering angle as

$$\frac{d\sigma_{\mathrm{B}}}{d\theta} = \frac{2\pi\alpha^2}{s}\frac{\sin\theta}{\sin^4(\theta/2)} \approx \frac{32\pi\alpha^2}{s}\frac{1}{\theta^3}. \tag{2.4}$$

According to Eq. (2.4), the highest number of Bhabha events is expected to be detected at the lowest polar angles. The resulting integrated cross section over an acceptance region defined between θ_{min} and θ_{max} is

$$\sigma_{\mathrm{B}} = \frac{16\pi\alpha^2}{s}\left[\frac{1}{\theta^2_{min}} - \frac{1}{\theta^2_{max}}\right]. \tag{2.5}$$

The formula in Eq. (2.3) applies to Bhabha scattering at low c.m.s. energies, for which γ exchange is the dominant process. At higher c.m.s. energies, the cross section for lowest order Bhabha scattering process includes γ and Z° exchange and may be presented as the sum of 10 terms [13]; three terms

identical to those presented in Eq. (2.3) and seven terms that describe contribution from s- and t-channel Z° exchange, and interference terms between these and the γ exchange. At this level, the contribution to the Bhabha scattering from weak interactions peaks at the Z° resonance mass [16], and grows with the scattering angle. Additional contributions to the Bhabha scattering cross section arise from higher order electro-weak radiative processes.

At present, the precision achieved in theoretical claculations of Bhabha scattering are believed to be of the order of 10^{-3} [17], well below the luminosity precision required for CLIC (comparable to the precision required at the ILC).

2.1.2 Beamstrahlung

In order to achieve high luminosity, the beams at the CLIC must have very small transverse dimensions at the interaction point. This leads to strong transverse electro-magnetic beam fields. In the case of electron positron collision, the field of each beam focuses the other beam, and the luminosity is enhanced. During the process of beam-focusing the beam-particles travel on curved trajectories, and therefore emit photons. This radiation is known as beamstrahlung. The average energy loss δE of a beam particle due to beamstrahlung is, in first approximation,

$$\delta E \propto \frac{N^2 \gamma_{\mathrm{L}}}{(\sigma_x + \sigma_y)^2 \sigma_z}, \tag{2.6}$$

where N is the number of bunch particles, γ_{L} is the particle Lorentz factor and $\sigma_x, \sigma_y, \sigma_z$ are the beam dimensions in x, y and z coordinates. Eq. (2.6) shows that the energy loss, and therefore the number of radiated photons, depends on the machine parameters and increases with decreasing beam dimensions [18].

2.1.3 Method and challenges

As stated in the beginning of this chapter, the integrated luminosity is calculated directly from the measured number of Bhabha scattering events. This number will be determined after applying a selection on the detected Bhabha events. The electromagnetic showers created by Bhabha particles in the forward- and in the backward-LumiCal will be reconstructed. The showers are required to be well-contained in the detector. A corresponding so-called

fiducial volume of the LumiCal is defined in terms of the incident electron polar-angle range. Provided the total energy deposited in the two arms of the LumiCal system is at least 80% of the nominal center-of-mass energy, a selection cut will be applied based on the collinearity of the e^+e^- candidates [2]. Complications are introduced by two physical phenomena described above, ISR and beamstrahlung. Both phenomena change the c.m.s. energy of the e^+e^- system from the nominal 3 TeV. The energy loss from beamstrahlung can be calculated from strong-field QED, but it strongly depends on beam parameters such as the bunch dimensions, beam position offsets and the details of the particle distributions in the bunches. These parameters are changing continuously during operation of the CLIC, and many of them cannot be measured directly. Differently from radiation induced by electroweak effects such as ISR and FSR which can be computed theoretically with high accuracy, the experimental effect of beamstrahlung radiation, and therefore the luminosity spectrum, must be determined through the measurement of a physics channel, in this case the Bhabha scattering. In addition, beam-beam interactions result in significant amount of background, i.e. hadrons originating from $\gamma\gamma$ interactions and low energy e^+e^- pairs (see chapter 4), in the detector and in particular in the LumiCal. Performing an efficient selection of Bhabha events is therefore a challenging mission.

Reconsruction of the luminosity spectrum may be carried out through a measurement of the acollinearity angle for the Bhabha e^+e^- final state, defined as $\theta_A = \theta_{e^-} + \theta_{e^+} - \pi$, where $\theta_{e^\pm}$ is the $e^\pm$ scattering angle. The acolinearity of Bhabha scattering is sensitive to the momentum imbalance between the interacting particles, which gives a good representation of the spread of the Bhabha c.m.s. collision energy [19].

Due to the fact that both ISR and beamstrahlung often occur assymetrically, meaning that one of the interacting leptons radiates more energy than its partner, the acollinearity of the final state can be significantly enhanced. Consequently, many events migrate outside of the defined angular acceptance region. The result is a reduction of the Bhabha events counting rate, also referred to as Bhabha suppression effect (BHSE). In the measurement of the luminosity, the loss of Bhabha events has to be corrected for. The correction can be calculated from the measured luminosity spectrum [20].

After the Bhabha scattering, the final state particles can be focused by the electromagnetic field induced by the opposite bunch space charge. This electromagnetic deflection (EMD) of the final state particles results in synchrotron radiation which is nearly collinear with the radiating particle. Both the beamstrahlung radiation and EMD effects lead to a reduction of the

number of Bhabha scattering events detected by the LumiCal in the defined experimental acceptance in comparison to the theoretically predicted one, and thus contribute to the BHSE. Previous studies done for the ILC conclude that relative to beamstrahlung, EMD effects do not modify significantly the luminosity spectrum [20]. EMD effects are not accounted for in this analysis.

2.2 The CLIC Experimental Environment

The CLIC bunch structure consists of 50 bunch trains per second, occurring at 20 msec time intervals. Each bunch train is 156 ns long and consists of 312 distinct bunch crossings (BXs), separated by 0.5 ns. The short time between bunches means that a detector will inevitably integrate over a number of BXs. This postulation makes beam related backgrounds even more significant. They have a major impact on the design of the inner region of the detector and the forward region in particular, and on the timing requirements placed on the individual detector elements.

In order to avoid near encounters of in- and outgoing bunches due to the presence of coherent pairs at small opening angles of a few milliradian (see Section 4.1), a crossing angle of 20 mrad is introduced between the two beam lines.

The BES of the CLIC beams is expected to be less than 0.5% [2]. It will be measured in an energy spectrometer upstream of the interaction point (IP).

2.2.1 The Luminosity Spectrum

As mentioned previously, not all the e^+e^- collisions at the CLIC will take place at the nominal c.m.s. energy, as the beam-particles may radiate a high-energy photon before their collision. Radiation due to beamstrahlung effect occurs prior to the hard Bhabha scattering. Consequently, the c.m.s. energy of the e^+e^- collision, $\sqrt{s'}$, may be less than the nominal c.m.s. energy of the machine $\sqrt{s}$. This results in an effective c.m.s. spectrum, the luminosity spectrum, with a peak at $\sqrt{s}$ corresponding to collisions with no radiation prior to the e^+e^- interaction and a long tail towards lower energies.

The normalized differential luminosity, $1/\mathrm{N}\,\mathrm{dN}/\mathrm{d}\sqrt{\mathrm{s}'}$, is shown in Fig. 2.2 for CLIC operating at $\sqrt{s} = 3\,\mathrm{TeV}$ as a function of the c.m.s. energy fraction,

$\sqrt{s'}/\sqrt{s}$. It is obtained from a sample of 5,396,614 e^+e^- pairs, simulated using the GuineaPig program [18] (see Section 3.1.2). The spectrum peaks at 3 TeV and a long tail due to beamstrahlung is evident.

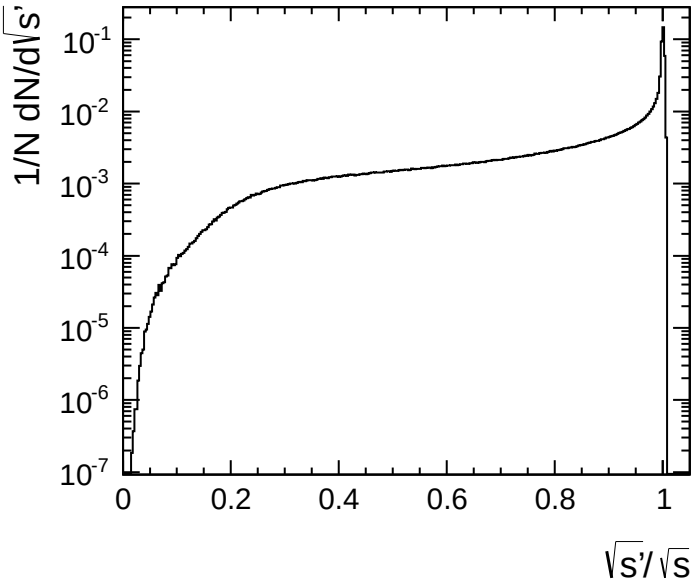

Figure 2.2: The normalized differential luminosity spectrum, $1/\mathrm{N}\,\mathrm{dN}/\mathrm{d}\sqrt{\mathrm{s}'}$, as a function of the c.m.s. energy fraction, $\sqrt{s'}/\sqrt{s}$.

2.3 The Luminosity Calorimeter

2.3.1 Calorimeters as Particle Detectors

Calorimeters are blocks of instrumented material in which particles to be measured are fully absorbed and their energy transformed into a measurable quantity. The interaction of the incident particle with the detector (through electromagnetic or strong processes) produces a shower of secondary particles with progressively degraded energy. Electromagnetic calorimeters are used mainly to measure incident electrons and photons through their electromagnetic interactions (e.g., bremsstrahlung, pair production). Sampling calorimeters consist of alternating layers of an absorber, a dense material used to degrade the energy of the incident particle, and an active medium

that provides the detectable signal. In solid-state sampling calorimeters, the signal is collected in the form of electric charge. The signal provided by the active part of the calorimeter serves as a measurement of the incident particle energy. It may also be used to determine the shower position and direction, and identify different particles on the basis of their different interactions with the detector [21].

The interaction of measured particles with the calorimeter material follows the physics principles of particles passage through matter. The fractional energy loss per radiation length (defined below) as a function of the electron energy is shown in Fig. 2.3a. At low energies electrons and positrons primarily lose energy by ionization, although other processes (Møller scattering, Bhabha scattering, e^+e^- annihilation) contribute. At high energies (above a few tens of MeV in most materials), bremsstrahlung losses dominate. Electron (positron) scattering is considered as ionization when the energy loss per collision is below 0.255 MeV, and as Møller (Bhabha) scattering when it is above.

The photon cross section in material is dominated by the photoelectric effect at low energies. Compton scattering, Rayleigh scattering, and photonuclear absorption contribute as well. As the energy increases, the probability for pair production to occur increases. This is shown in Fig. 2.3b, where the probability that a photon interaction will result in conversion to an e^+e^- pair is plotted as a function of the photon energy, for several materials as indicated in the figure.

Electromagnetic Showers

When a high energy electron hits a block of material it starts a cascade process, known as electromagnetic shower. The developement of the shower starts when the incoming electron emits a bremsstrahlung photon. Assuming the photon energy is sufficiently high, it will in turn convert into an electron-positron pair, and the pair partners will then each perform bremsstrahlung, and so forth. The cascade process will continue until the secondary particles reach a critical energy [2] ϵ, below which no further multiplication occurs. From that point, the electrons (photons) proceed to lose their energy due to, mainly, ionization and thermal excitations (Compton scattering and photoelectric absorption) [21].

[2] ϵ is defined as the energy at which the rate of energy loss per radiation length equals the total energy of the electron

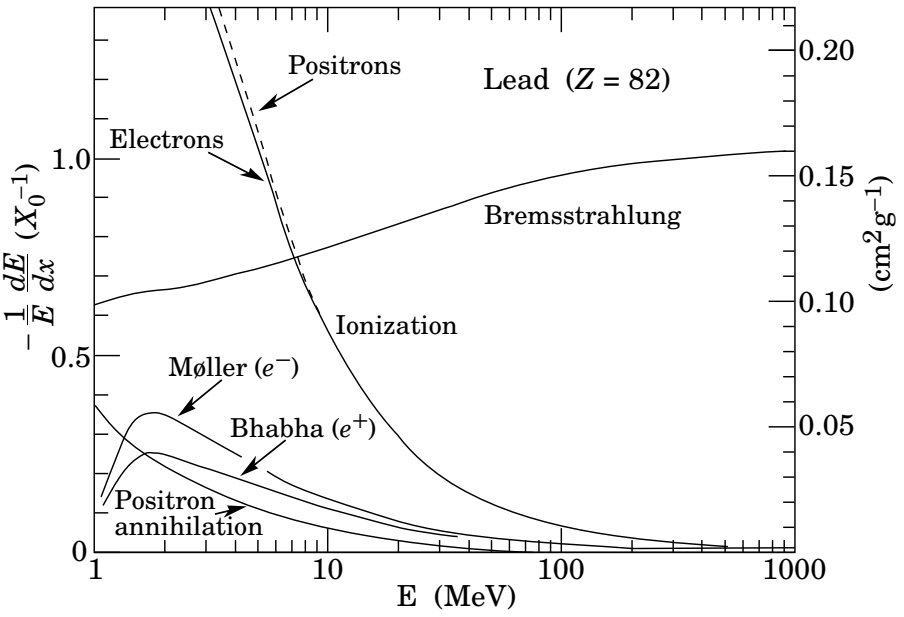

(a)

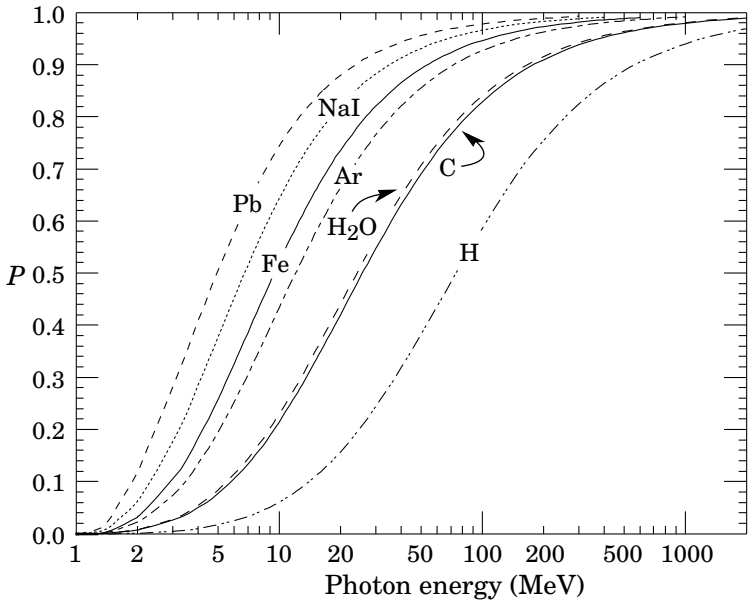

(b)

Figure 2.3: (a) Fractional energy loss per radiation length in lead as a function of electron or positron energy. (b) Probability P that a photon interaction will result in conversion to an e^+e^- pair (the figures are taken from [22]).

The scale for the lungitudinal distribution of the shower is set by the radiation length X_0, usually measured in $\mathrm{g\,cm^{-2}}$, which is both the mean distance over which a high-energy electron looses all but $1/e$ of its energy by bremsstrahlung, and 7/9 of the mean free path for pair production by a high-energy photon. The transverse size of an electromagnetic shower is mainly due to multiple scattering of electrons and positrons away from the shower axis. A measure of the transverse size, integrated over the full shower depth, is given by the Molière radius (R_M), which can be approximated by $R_M \simeq 21\,MeV\ X_0/\epsilon(\,\mathrm{MeV})$ [21]. On average, about 90% of the shower energy is contained in a cylinder of radius $\sim 1R_M$.

2.3.2 The LumiCal Design

LumiCal is a sampling calorimeter, with tungsten as absorber and silicon sensors as the active medium. The Calorimeter is in a form of a barrel which is divided into two arms along the vertical plane. On both sides of the interaction point there will be one LumiCal detector. In CLIC, the front face of LumiCal is placed 2.6 m from the interaction point (IP). LumiCal is centered on the outgoing beam axis and is tilted relative to the detector symmetry axis to be perpendicular to the beam. The LumiCal inner radius is 10 cm, and its outer radius is 29 cm, resulting in a polar angular coverage of 37.5 to 109 mrad. The calorimeter consists of 40 layers. Each layer is made up of a 3.5 mm thick tungsten disk, which is equivalent to $1\,\mathrm{X_0}$. Behind each tungsten layer there is a 0.2 mm ceramic support, a 0.32 mm silicon sensor plane, and a 0.25 mm gap for electronics. The tungsten disks are precisely positioned using 4 bolts which are stabilised by additional steel rings on both sides of the cylinder. The transverse plane is subdivided in the radial and azimuthal directions. The basic unit of each sensor plane is a silicon sensor tile, shown in Fig. 2.4b, designed by the FCAL collaboration and custom fabricated by the Hamamatsu Corporation. Each sensor plane consists of 12 such tiles. The number of radial divisions in a sensor plane is 64, and the number of azimuthal divisions is 48. In total, each LumiCal will have 92,160 electronic readout channels. The Molière radius of electromagnetic showers in the LumiCal is 1.1 cm [12]. Figure 2.4a presents the mechanical structure of LumiCal.

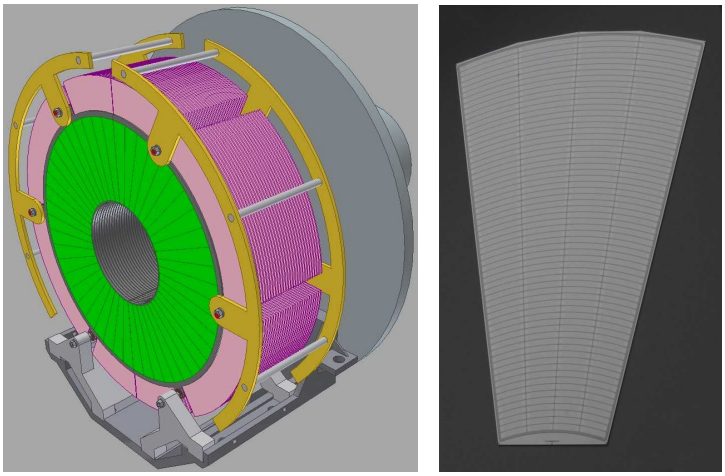

(a) (b)

Figure 2.4: (a) The mechanical structure of LumiCal. (b) One of the Hamamatsu silicon-sensor tiles.

First test-beam measurements of the LumiCal silicon-sensor prototype with a full readout chain [23] were performed in the summer of 2010 by the FCAL collaboration. Description of the test-beam setup and analysis of these measurements may be found in [23, 24, 25].

The design of the LumiCal front-end electronics may be found in reference [26]. The front-end will work in two modes, the physics mode and the calibration mode. In the physics mode the detector should be sensitive to electromagnetic showers resulting in high energy deposition and the front-end should process signals up to about 10 pC per channel [26]. In the calibration mode it should detect signals from relativistic muons, i.e. it should be able to register minimum ionizing particles (MIPs). It means that signals as small as 2 fC (corresponding to the low-end of the Landau distribution for MIPs in 300 μm thick silicon) should be detected.

2.4 Uncertainties of the Luminosity Measurement

There are several contributions to the relative uncertainty of the luminosity measurement. Here they will be classified as statistical (subscript *stat*) and

systematic uncertainties (subscript *rec*), where the latter originate mostly from the reconstruction process,

$$\frac{\Delta\mathcal{L}}{\mathcal{L}} = \left(\frac{\Delta\mathcal{L}}{\mathcal{L}}\right)_{stat} \oplus \left(\frac{\Delta\mathcal{L}}{\mathcal{L}}\right)_{rec} . \tag{2.7}$$

The statistical contribution follows from the fact that the luminosity is measured with a statistical uncertainty in the counting of N_B (defined in Eq. (2.1)), and may be expressed as

$$\left(\frac{\Delta\mathcal{L}}{\mathcal{L}}\right)_{stat} = \frac{1}{\sqrt{N_B}}. \tag{2.8}$$

The distribution of the differential Bhabha cross section as a function of the electron scattering angle, $d\sigma/d\theta$, was obtained from the BHWIDE generator (see chapter 3) for c.m.s. energy of 3 TeV, and it is shown in Fig. 2.4. Radiative effects such as ISR and FSR are included. Within the LumiCal geometrical volume, the physical Bhabha cross-section is 101.016 pb. Assuming a luminosity of $5.9 \cdot 10^{34}\,\mathrm{cm}^{-2}\,\mathrm{s}^{-1}$, a rate of 5.96 Hz is expected, which approximately translates into one Bhabha scattering event for every 10 bunch trains. As discussed later in Section 3.2.1, the requirement of shower containment for the Bhabha scattering final states and the scattering off the ECal edge limit the fiducial volume to the range 44 mrad to 80 mrad (see vertical lines in Fig. 2.4), which corresponds to a cross section of 62 pb. Assuming an integrated luminosity of $500\,\mathrm{fb}^{-1}$ per year, this translates into a relative statistical precision on the Bhabha scattering yearly rate of $1.8 \cdot 10^{-4}$, well below the requirement of 1%.

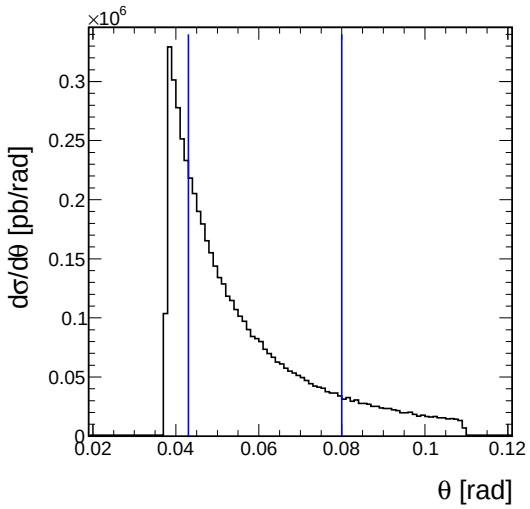

Figure 2.5: Cross section of the Bhabha process as a function of the electron polar angle, θ, obtained from the BHWIDE [27] generator. The vertical lines at $\theta = 44\,\text{mrad}$ and $\theta = 80\,\text{mrad}$ mark the fiducial volume limits.

The reconstruction uncertainty in Eq. (2.7) originates from the uncertainty on the correction applied to N_{sel}, the measured number of Bhabha events that passed the selection cuts described in Section 2.1.3. This correction, formulated below in Eq. (2.9), is based on Monte Carlo (MC) simulations. The idea of the correction is to compensate for the difference registered in MC simulations between the number of generated Bhabha events expected for a certain luminosity, N^L_{gen}, and the number of events which passed the selection cuts, N^{MC}_{sel}, for the same luminosity. The corrected number of real-life reconstructed events is then

$$N_B = N_{sel}\left(\frac{N^L_{gen}}{N^{MC}_{sel}}\right), \tag{2.9}$$

meaning that the uncertainty on N^{MC}_{sel} contributes directly to the uncertainty on the measured luminosity. Additional contributions to the uncertainty on the luminosity comes from the uncertainty on N_{sel} due to uncertainties on energy- and polar angle reconstruction, as discussed below.

The requirement for the total energy measured in the LumiCals to be larger than 80% of the c.m.s. energy was introduced in Section 2.1.3 as a

selection criteria for Bhabha events. The measured energy is in fact the measure of charge collected in the calorimeter scaled by a factor known as the energy scale. The energy scale is obtained from beam tests and from the reconstructed luminosity spectrum in the process of in-situ energy calibration, as discussed in Section 3.3. A bias in the energy scale implies a bias in the number of selected Bhabha events and hence a contribution to the uncertainty in the measured luminosity.

In order to estimate the contribution of the uncertainty in the energy scale to the uncertainty in N_B, the integrated luminosity spectrum is examined. By integrating over the luminosity spectrum, one obtains the total number of Bhabha scattering events for which the c.m.s. energy fraction is higher than 80%.

The parameter $f_{int}(\sqrt{s'})$ is defined here as the fraction of events in the luminosity spectrum with c.m.s. energy higher than $\sqrt{s'}$ and it is shown in Fig. 2.6 as a function of the c.m.s. energy fraction, in the area around $\sqrt{s'}/\sqrt{s} = 0.8$. It is now possible to calculate the variation in the number of selected Bhabha events, N_B, as a function of a variation in the energy scale factor, and vice versa. The variation in the c.m.s. energy fraction due to a variation of 10^{-2} in $f_{int}(\sqrt{s'})$ defines an upper bound for the energy scale uncertainty. In the vicinity of $\sqrt{s'}/\sqrt{s} = 0.8$, $f_{int}(\sqrt{s'})$ is to a good approximation linear. A linear fit, shown in Fig. 2.6, was applied in the range $0.796 < \sqrt{s'}/\sqrt{s} < 0.804$. The slope was found to be equal to -0.95. This leads to the conclusion that at the CLIC, to achieve a precision of 10^{-2} in counting the Bhabha events, the energy scale uncertainty has to be below 0.9%.

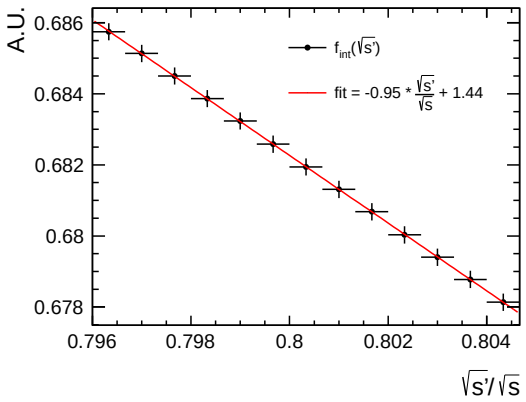

Figure 2.6: The fraction of events in the luminosity spectrum with c.m.s. energy higher than $\sqrt{s'}$, $f_{int}(\sqrt{s'})$, as a function of the c.m.s. energy fraction, $\sqrt{s'}/\sqrt{s}$ (black dots). The linear fit (red line) and its results are indicated in the figure.

Energy deposits from beam-related background is added to the electron energy deposits in the LumiCal. It is rather simple to correct the measured electron energy by subtracting the background energy deposits averaged over BXs. However, since the background energy deposits per BX fluctuate, an unavoidable contribution to the relative uncertainty in energy is introduced. As a result, the energy resolution of the LumiCal as Bhabha detector detriorates, and the relative uncertainty in luminosity increases, depending on the number of integrated BXs. The energy resolution of the LumiCal in presence of background was studied, and the results are discussed in chapter 5.

The other selection criterion introduced in Section 2.1.3 concerns the polar angle reconstruction. Since the integrated cross section falls as $1/\theta^2$ (see Eq. (2.5)), the luminosity shift as a function of the polar angle bias can be expressed as

$$\frac{\Delta\mathcal{L}}{\mathcal{L}} \approx \frac{2\Delta\theta}{\theta_{min}} \tag{2.10}$$

where θ_{min} is the minimum polar angle of the fiducial volume and $\Delta\theta$ is a bias to the polar angle measurement. A bias in the polar angle may also rise from systematic uncertainty of the radial or longitudinal position of the reconstructed shower. For LumiCal to achieve an accuracy of 10^{-2} in the measured luminosity, the uncertainty of bias on the angular reconstruction has to be smaller than 0.2 mrad.

This implies that the inner calorimeter radius of 100 mm must be known with a precision of better than 0.5 mm, and the position of the LumiCal along the beam line has to be known to within 13 mm. These requirements will be answered with the proposed granularity and the fact that the position of the LumiCal will be monitored with a laser system which will provide sensitivity to longitudinal displacements of 100 μm [2].

Other contributions to the uncertainty in luminosity measurement may be found in [28].

The results of this chapter are summarized in Table 2.1.

Summary of luminosity measurement parameters and uncertainties			
		Prediction	Requirement
Assumed experiment parameters	$\sqrt{s}$	3 TeV	–
	$\mathcal{L}_{\text{int}}$	$500\,\text{fb}^{-1}$/year	1%
Results from simulations	Bhabha cross section within f.v.[a]	62 pb	–
	Bhabha events rate expected in f.v.	5.96 Hz	–
	stat. uncert. on Bhabha yearly rate	0.018%	1%
	uncert. on LumiCal energy scale	see Section 3.3.2	0.9%
	uncert. on polar angle reconst.	0.02 mrad	0.2 mrad
	uncert. on position along beam-line	~ 0.1 mm	13 mm
	uncert. on inner radius of LumiCal	~ 0.1 mm	0.5 mm

Table 2.1: Summary of the luminosity measurement parameters and uncertainties.

[a]Here f.v. stands for fiducial volume, see Section 3.2.1

Chapter 3

The Performance of LumiCal

3.1 Simulation Tools

3.1.1 Detector simulation

The response of LumiCal to the passage of particles was simulated using MOKKA [29]. The software framework MOKKA is an application of a general purpose detector simulation package, GEANT4 [30]. The detector model chosen for MOKKA was CLIC_ILD_CDR[1], where LumiCal is constructed by the LumiCalX super driver, and the geometry of LumiCal which was simulated is that which is described in Section 2.3. The current simulation of the detector does not include realistic features of the calorimeter, such as in-active material at the inner and outer radii of LumiCal. The output of MOKKA is in the LCIO format, which may be processed by MARLIN, a C++ software framework for the ILC software [31]. It can be used for all tasks that involve processing of LCIO files, e.g. reconstruction and analysis. Several MARLIN processors (modules) were written in order to analyze the LCIO output.

The MOKKA program provides values of measured energy in a scale referred to as *detector units*, corresponding to the amount of energy lost in the active material, silicon in the case of LumiCal. In order to translate the

[1]This detector model was used for all studies done as a part of the CLIC CDR, as explained in Section 1.2.

energy signal into units of charge, the following formula is used:

$$\mathrm{SQ[fC]} = \frac{1.6 \cdot 10^{-4}}{3.67}\mathrm{SE[eV_d]}\,, \tag{3.1}$$

where SE denotes the signal expressed in *detector* eV, also denoted by $\mathrm{eV_d}$, and SQ the signal in units of fC. The value 3.67 eV is the energy to create an electron-hole pair in silicon. The number $1.6 \cdot 10^{-4}$ fC is the electric charge of the electron [12].

3.1.2 Event generators

Bhabha scattering events were generated using BHWIDE [27]. BHWIDE is a wide-angle Bhabha MC simulation program that contains the electroweak contributions, which are important for the high energy e^+e^- interactions considered here. The spectrum of the c.m.s. energy of Bhabha events presented in Section 3.3 was obtained using GuineaPig [18], a simulation program for beam-beam interactions at e^+e^- colliders. Given certain beam parameters, GuineaPig simulates ISR and beam-beam interactions. The GuineaPig output is a list of the four-momenta of all the beam-particles predicted to undergo interactions.

3.2 Energy Resolution

The measurement of energy with an electromagnetic calorimeter is based on the principle that the energy released in the detector material by the charged particles of the shower, mainly through ionization and excitation, is proportional to the energy of the incident particle. The total track length of the shower, defined as the sum of all ionization tracks due to all charged particles in the cascade, is proportional to the number of particles in the shower. This number can be estimated as E_0/ϵ, where E_0 is the original particle energy, and ϵ is the critical energy (defined in 2.3.1) [21]. The measurement of the signal produced by the charged tracks of the electromagnetic cascade provides a measurement of E_0. Since the total track length is proportional to the number of track segments in the shower and the shower development is a stochastic process, the intrinsic energy resolution is given, from purely statistical arguments, by $\sigma(E) \propto \sqrt{E}$, where σ and E are the standard deviation and the mean of the deposited energy distribution (which is Gaussian-like), respectively.

For realistic (non-ideal) calorimeters, a general parametrization of the fractional energy resolution is

$$\frac{\sigma}{E} = \frac{a}{\sqrt{E}} \oplus \frac{b}{E} \oplus c, \tag{3.2}$$

where $\oplus$ indicates a quadratic sum, a is called the *stochastic term*, b is called the *noise term* and c is called the *constant term*. The stochastic term represents statistics-related fluctuations that emerge from the physical development of the shower, as discussed above. The noise term contribution to the energy resolution comes from the electronic noise of the readout chain and depends on the detector technique and on the features of the readout circuit. The constant term includes contributions from nonuniformities in the calorimeter response, caused by instrumental effects.

In sampling calorimeters the energy deposited in the active medium fluctuates event by event, due to variations in the number of charged particles that cross the active layers. These so called *sampling fluctuations* represent the intrinsic limitation to the energy resolution of these calorimeters. In the simulation used for this analysis, the terms b and c in Eq. (3.2) are not expected to appear, as the detector simulation does not include gaps in the active material or readout electronics digitization. Therefore a dependence of the resolution of the form

$$\frac{\sigma}{E} = \frac{a_{res}}{\sqrt{E}} \tag{3.3}$$

is assumed, where a_{res} is the intrinsic energy resolution parameter, given in $\sqrt{\text{GeV}}$.

3.2.1 The energy resolution of the LumiCal

In order to calculate the energy resolution parameter of the calorimeter, the response of the LumiCal within the full CLIC ILD detector model was simulated. The incident particles were chosen to be 1.5 TeV electrons with impact angles uniformly distributed over the LumiCal geometrical volume ($37.5 - 109$ mrad). Here impact angle is defined as the polar angle of the incident electron, defined as the angle between the beam direction and the electron momentum vector. A sample of 160,000 such electrons was generated.

For every electron, the total deposited energy was obtained by summing over all of the LumiCal pads. The impact angle range covered by the LumiCal was divided to bins. For each bin, the mean and RMS of the total

energy distribution, E_{mean} and σ_e respectively, were estimated by applying a Gaussian fit. Following Eq. (3.3), the energy resolution parameter is given by

$$\frac{a_{res}}{\sqrt{E_b}} = \frac{\sigma_e}{E_{mean}} \tag{3.4}$$

where $\sqrt{E_b}$ is the beam energy, given in GeV. In the following, a_{res} will be referred to as the energy resolution of the LumiCal.

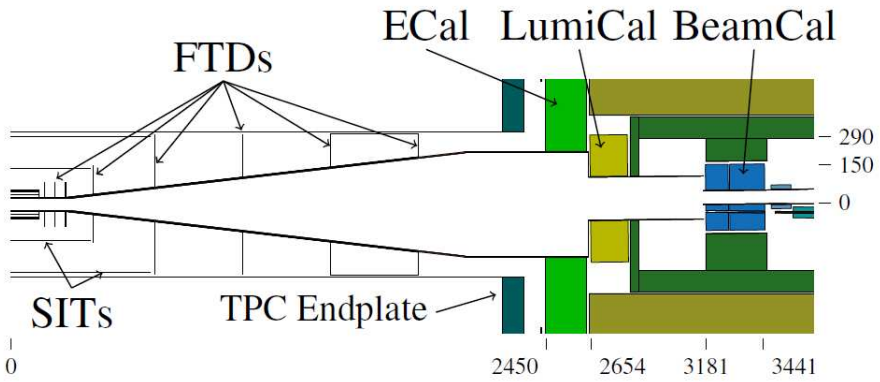

Figure 3.1: Forward tracking and calorimeters seen from the top.

A detailed scheme of the forward region layout of the CLIC ILD detector (Fig. 1.3) is shown in Fig. 3.1, where it is evident that ECal partially covers the front-face of the LumiCal. Due to this overlap, the Bhabha scattered particles may pre-shower before entering the LumiCal. The correlation between N_{hit}, the number of LumiCal pads hit by the electromagnetic shower particles and θ_{gen}, the generated polar impact angle of the electron, is shown in Fig. 3.2.

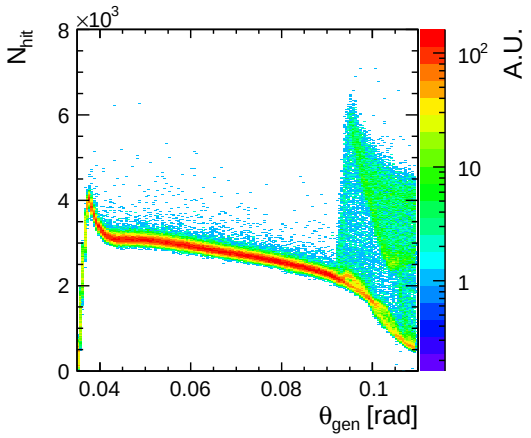

Figure 3.2: The correlation between the number of pads hit by an incident electron, N_{hit}, and its polar incident angle, θ_{gen}.

As expected, N_{hit} rises sharply as θ_{gen} increases from 37 mrad, the inner edge of the LumiCal, to 44 mrad, the inner edge of the LumiCal fiducial volume. In the region between 44 mrad and 90 mrad N_{hit} decreases moderately due to the difference in pad sizes between the inner- and outer- radii of the LumiCal silicon sensor tiles (see Fig. 2.4b). A clear increase in the fluctuations of the number of pads is observed at 90 mrad, corresponding to the overlap between the calorimeters. Shown in Fig. 3.3 is the energy resolution as a function of the generated impact angle of the electron, θ_{gen}. The error bars are derived from the uncertainty on the fits of the value of σ_e, from which a_{res} was extracted. The energy resolution is minimal and stable around a value of $0.21\sqrt{\text{GeV}}$ within the angular range of $44 - 80$ mrad. This implies that the electromagnetic shower developed by incident 1.5 TeV electrons with impact angle in the above range, defined as the fiducial volume of the LumiCal, is well-contained in the detector. The nominal intrinsic LumiCal energy resolution, averaged over the angular range of the fiducial volume, for measurement of 1.5 TeV particles, is esimated to be $a_{res} = 0.2098 \pm 0.0004\sqrt{\text{GeV}}$ in the fiducial volume. The resolution deteriorates below 44 mrad due to leakage and above 80 mrad due to the detector geometry described above. During the operation time of the accelerator, the recorded hit data shall be used for reconstruction of the incident electrons impact angle. Electrons with impact angle that exceeds the limits of the fiducial volume will not be counted for the integrated luminosity measurement.

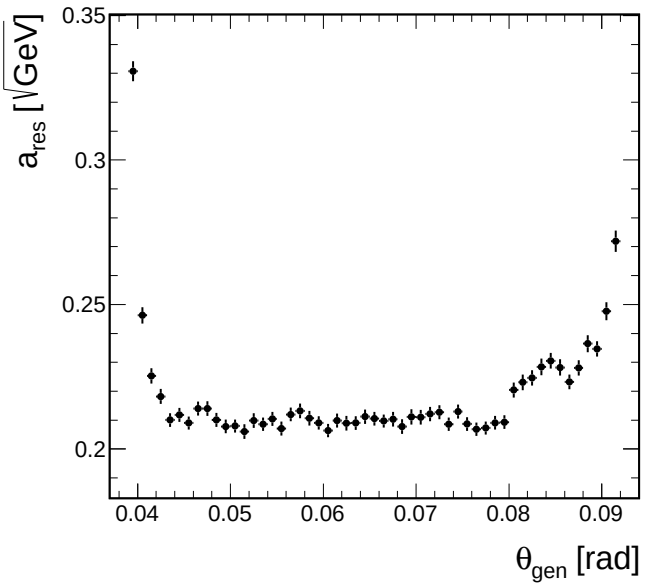

Figure 3.3: Measure of the energy resolution, a_{res} , as a function of the e^- generated angle, θ_{gen}.

3.2.2 Proposed method for deriving the LumiCal energy resolution in-situ

During the data taking in the real experiment, the method used in the previous section to determine the energy resolution is not applicable. However, the energy resolution of the detector may also be estimated as follows: inject two back-to-back particles with known energy, in this case 1.5 TeV electrons, into both LumiCals; extract a distribution of the difference between the measured energies in the right- and left LumiCal and apply a Gaussian fit; the width of this distribution is expected to be equal to $\sqrt{2}\sigma_e$. The most probable value (MPV) of the distribution of total energy deposited summed over both LumiCals, $E_{3\,\text{TeV}}$, may be found by applying a Gaussian fit. The value of $E_{3\,\text{TeV}}$ is expected to be equal to twice the MPV of energy deposited in the LumiCal by a 1.5 TeV electron.

This method was applied here by injecting 60,000 back-to-back e^+e^- pairs, with polar angles within the range of the LumiCal fiducial volume

defined above, into the full detector simulation. The resulting parameters, $E_{3\,\mathrm{TeV}}$ and $\sigma_{3\,\mathrm{TeV}}$, are given in the *detector units* denoted by $\mathrm{GeV_d}$, defined in the beginning of this chapter (see Eq. (3.1)). Their values are $36.97\,\mathrm{GeV_d}$ and $0.14\,\mathrm{GeV_d}$, respectively, and are known to a very good precision. The energy resolution coefficient obtained in this method is as expected $a_{res} = 0.21\,\sqrt{\mathrm{GeV}}$. The average energy deposited by a 1.5 TeV electron in the LumiCal corresponds to $18.48\,\mathrm{GeV_d}$. This means that the reconstructed energy deposited by such incident electron in the LumiCal is Gaussian-like distributed with a width of 8 GeV.

This method for deriving the intrinsic energy resolution of the LumiCal can be implemented in-situ by requiring strict cuts on the colinearity of the Bhabha scattered particles. Assuming an integrated luminosity of $500\,\mathrm{fb}^{-1}$ and a cross section of 62 pb within the LumiCal fiducial volume (see Section 2.4), 80,000 Bhabha events will be accumulated during one day of the machine operation. In practice the uncertainty in the energy resolution will depend on other factors as well, e.g. the readout electronics system. It is also important to note that the detector simulation MOKKA is not fully detailed; for example, gaps between sensor tiles and sections are not take into account. The electronics noise and the structural details contribute to the width of the electromagnetic shower signal and increase the energy resolution, in particular the coefficients b and c are non-zero.

3.3 In-Situ Energy Calibration

Calorimeter calibration has several purposes; to equalize the cell-to-cell output signals in order to obtain a response as uniform as possible and therefore a small contribution to the constant term of the energy resolution; to set the absolute energy scale for the incident particles; to monitor variations in the detector response with time. Three main tools are usually employed to calibrate a calorimeter; hardware-, test beam- and in-situ calibration.

In order to perform hardware calibration, the electronics-calibration-system injects a known pulse at the input of the readout chain. This calibration process allows to monitor the cell-to-cell response of the detector and to minimize the discrepancies between the channels of the readout chain. In test-beam calibration, calorimeter modules are exposed to test beams before being installed in the final detector. Given that the energy of the test-beam is well known, this calibration process allows to set a preliminary absolute energy scale for incident particles and to check the linearity of the response of the

full chain.

The in-situ calibration is a further calibration step needed after installation of the calorimeter in the experiment. It allows one to correct residual nonuniformities, to understand the impact of the upstream material and of the experimental environment, to follow the detector response variations with time, and to set the final absolute energy scale under experimental conditions. The latter is one of the most challenging steps of the calorimeter calibration procedure. At e^+e^- colliders the precise knowledge of the c.m.s. energy provides useful constraints and in principle renders this operation easier.

The process of in-situ calibration tested in this analysis consists of four steps.

1. Obtain the luminosity spectrum from GuineaPig.
2. Generate a sample of Bhabha scattering events with c.m.s. energies that correspond to the luminosity spectrum.
3. Pass the Bhabha particles through the full detector simulation, MOKKA.
4. Reconstruct the luminosity spectrum and locate the position of the peak.

The GuineaPig provides the momenta of both leptons prior to the physical interaction (Bhabha scattering). The Bhabha scattering is simulated in the c.m.s. frame, where the leptons momenta are equal in absolute value and opposite in direction. After generation of Bhabha events with various c.m.s. energies, the final state particles of each event are boosted from the c.m.s. to the laboratory system. In the MOKKA simulation program a rotational boost is performed from the lab system to the detector system, as implementation of the incoming beams crossing angle.

3.3.1 Reconstruction of the luminosity spectrum

During the operation time of the accelerator, the reconstruction of the c.m.s. energy will become a more complex assignment which includes a clustering algorithm for the shower reconstruction as well as background subtraction. In this chapter, the analysis of the input for the detector consists only of Bhabha events, therefore a simplified approach is taken. The reconstructed c.m.s. energy of each Bhabha event is obtained by summing over the energy deposits in all of the detector pads, in both LumiCals. In this method, the

reconstructed c.m.s. energy is expected to consist of the outgoing leptons energy and the radiation which accompanies them, FSR and synchrotron radiation (the latter is due to EMD). This means that c.m.s. energy of events in which ISR occurred can not be fully reconstructed from the LumiCal.

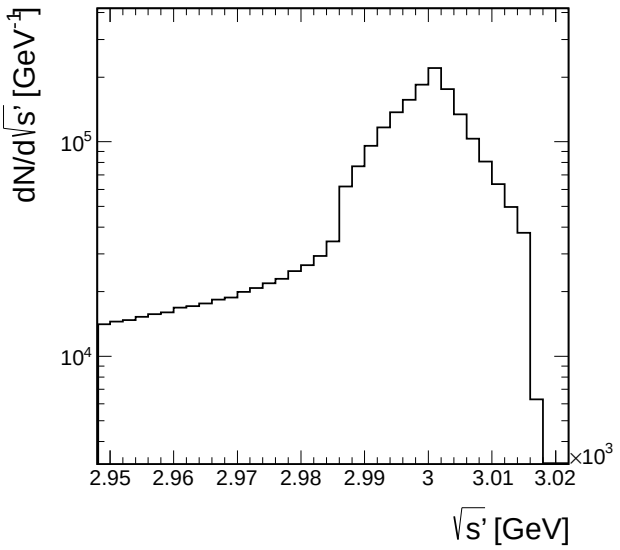

Figure 3.4: The normalized differential luminosity, $1/N\, dN/d\sqrt{s'}$, as a function of the c.m.s. energy, $\sqrt{s'}$, zoomed around the peak area.

The area around the peak of the generated luminosity spectrum is shown in Fig. 3.4. Ideally, a sharp fall to zero events above $\sqrt{s'} = 3\,\text{TeV}$ in the luminosity spectrum is expected. However, the inherent BES in CLIC results in a different peak-structure which can be approximated by a logarithmic decay. The width of the peak-structure is about 10 GeV, while the LumiCal energy resolution at the peak energy is expected to be $\sqrt{2}{\cdot}8\,\text{GeV} = 11.3\,\text{GeV}$. This means that the BES and the smearing due to the LumiCal intrinsic energy resolution have approximately the same width; therefore if the BES was Gaussian-like distributed, the width of the peak would be expected to grow by an extra factor of about $\sqrt{2}$ relative to σ_e (defined in Section 3.2.1).

The sample of events from which the luminosity spectrum is reconstructed consists of $4.6 \cdot 10^6$ simulated Bhabha scattering events, with varying c.m.s. energy corresponding to the normalized differential luminosity shown in Fig. 2.2.

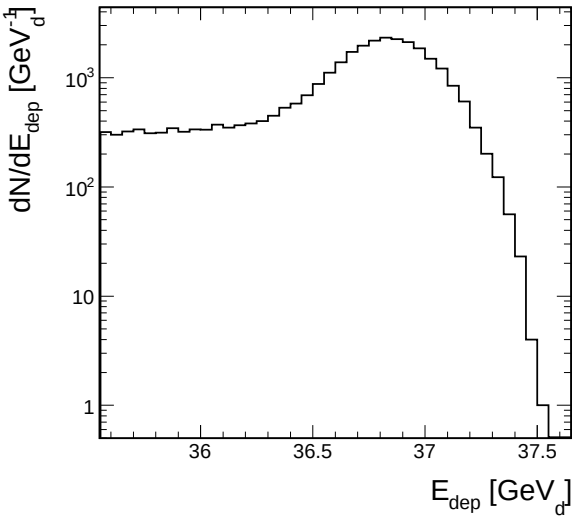

Figure 3.5: The peak area of the reconstructed luminosity spectrum, dN/dE_{dep}, as a function of the energy deposited in detector units, $\mathrm{GeV_d}$, in both LumiCal arms summed over all pads, E_{dep}.

The sample contains only events in which the leptons are scattered within the polar angular range $20 < \theta < 135\,\mathrm{mrad}$. A fiducial volume cut was applied, so that events in which the polar angle of one or both leptons was not within the angular range of $44 - 80\,\mathrm{mrad}$ were discarded, in order to avoid energy leakage. The peak area of the reconstructed luminosity spectrum, dN/dE_{dep} is shown in Fig. 3.5 as a function of the energy deposited in both LumiCal arms, summed over all pads, E_{dep}. The reconstructed spectrum peaks around $36.85\,\mathrm{GeV_d}$ and falls by one order of magnitude within a range of about $0.2\,\mathrm{GeV_d}$ around the peak.

3.3.2 Calibration Performance

Calibration using cumulative Gaussian fit

The MPV of the reconstructed luminosity spectrum, E_{reco}, is identified with the nominal c.m.s. energy, 3 TeV. If the reconstructed energy of an event is higher than the nominal, it is assumed to be due to the BES and the

smearing caused by LumiCal energy resolution. As a simplified approach, the area to the right of E_{reco} in the reconstructed spectrum is assumed to be Gaussian-like distributed, with a width denoted by σ_{reco} that encompasses both BES and energy resolution. The area to the left of E_{reco} encompasses the luminosity spectrum shape as well as the smearing effects. Following that logic, the Gaussian-like distribution describes well only the area to the right of E_{reco}, unlike the area to the left of E_{reco}, where the Gaussian is distorted by the luminosity spectrum shape. Therefore, in order to locate the peak of the reconstructed luminosity spectrum and determine the energy scale, it is advisable to perform a cumulative Gaussian fit using the complementary error function, rather than a simple Gaussian fit. The fit should be done keeping in mind that the bins of the cumulative spectrum are correlated.

The cumulative reconstructed spectrum, dN_c/dE_{dep}, is defined as the integration over the reconstructed luminosity spectrum, from ∞ to E_{dep}. The lowest value of E_{dep} in the cumulative reconstructed spectrum shall be denoted by E_{cutoff}. The value of E_{cutoff} needs to be chosen so that dN_c/dE_{dep} is defined within the Gaussian-like distributed area of dN/dE_{dep}. The objective is to perform a reliable fit while keeping the condition $E_{cutoff} \gtrsim E_{3\,\text{TeV}}$, where $E_{3\,\text{TeV}}$ was defined previously (see Section 3.2.2). The process of choosing the optimal value of E_{cutoff} was done here in two steps, as described in the following.

First, an initial value was chosen for E_{cutoff}. The results of the cumulative Gaussian fit to dN_c/dE_{dep} when the cutoff point is chosen to be $E_{cutoff} = 0.99 \cdot E_{3\,\text{TeV}}$, are summarized in Table 3.1. The MPV value of the reconstructed luminosity spectrum, E_{reco}, and $E_{3\,\text{TeV}}$ differ by $0.12 \pm 0.0015\,\text{GeV}_\text{d}$. This difference, which is statistically significant, most probably originates from the distortion of the Gaussian shape by the non-Gaussian distribution of BES. This systematic effect is of about 0.33% and can be corrected in the process of calibration. As expected, due to the BES and the shape of the luminosity spectrum, the value of σ_{reco} is higher than $\sigma_{3\,\text{TeV}}$. They differ by a factor of 1.4.

single electrons		luminosity spectrum		units
$E_{3\,\mathrm{TeV}}$	36.96	E_{reco}	36.84	$\mathrm{GeV_d}$
$\sigma_{3\,\mathrm{TeV}}$	0.14	σ_{reco}	0.20	$\mathrm{GeV_d}$

Table 3.1: Summary of the cumulative Gaussian fit results, E_{reco} and σ_{reco}, quoted in units of *detector* GeV, $\mathrm{GeV_d}$. Also shown are the values of the same parameters, from single-electrons analysis (see Section 3.2.2). The relative uncertainties are purely statistical and are of the order of $\mathcal{O}(10^{-2})$ at most.

Next, the value of E_{cutoff} was increased constantly in small-size steps. For convenience, the cutoff point with reference to $E_{3\,\mathrm{TeV}}$ in units of σ_e, C_σ, is defined as follows:

$$C_\sigma = \frac{E_{cutoff} - E_{3\,\mathrm{TeV}}}{\sigma_{3\,\mathrm{TeV}}}. \tag{3.5}$$

The cumulative Gaussian fit was performed for different cutoff points, in the range $-3 < C_\sigma < 2$. As the cutoff point increases, the fit parameters values diverge from the values presented in Table 3.1. The relative peak difference, Δ_{MPV}, defined as the ratio $\frac{E_{\mathrm{reco}} - E_{3\,\mathrm{TeV}}}{E_{3\,\mathrm{TeV}}}$, is shown in Fig. 3.6a as a function of the cutoff point, C_σ, with error bars that indicate the uncertainty. The value of Δ_{MPV} increases slowly in the range $-3 < C_\sigma < -1$, which demonstrates the distortion of the peak due to the luminosity spectrum shape. In the range $-1 < C_\sigma < 0$ it is almost stable, around the value $\Delta_{\mathrm{MPV}} = -0.25 \pm 0.02\%$, where the uncertainty in the bias is estimated here as the difference between the maximum and minimum values of Δ_{MPV} in this range. For $C_\sigma > 0$ it is again unstable. The uncertainties grow as the statistics decrease, meaning as C_σ increases. To conclude, a bias in the energy scale towards values smaller than the expected is seen, but generally the value of the energy scale obtained in this method is unstable.

In this case, there is no advantage to the cumulative Gaussian fit over the Gaussian fit, and the simplifying assumption made in the beginning of 3.3.2 is not valid. This method will therefore be rulled out in this analysis. It will be pointed out here that one may still perform such calibration, using the stable area of Δ_{MPV}. The bias should then be corrected for, and its value and uncertainty are still significantly lower than the requirement on the accuracy of the energy scale (see Section 2.4).

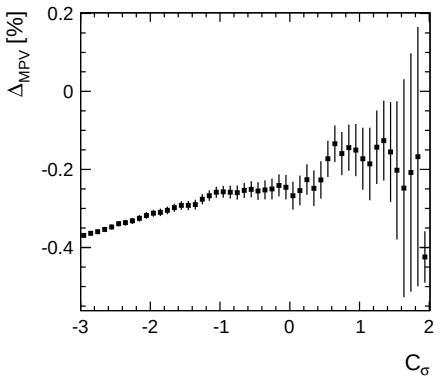

(a)

Figure 3.6: The relative peak difference, Δ_{MPV} as a function of the cutoff point, C_σ.

Model-independent calibration method

Given that the peak structure of the luminosity spectrum is shaped in a functional form which is non-trivial to fit and unfold, an alternative method of locating and estimating the uncertainty of the reconstructed luminosity spectrum peak is proposed, in which no assumptions regarding the peak structure are made. The numerical method of finding the MPV of a certain distribution without assuming any particular functional shape is to derive the distribution, and find the point at which the derivative intersects the variable axis. In the case of the luminosity spectrum neighboring bins are correlated, and these correlations needs to be taken into account when estimating the uncertainty in the MPV location. A simple way to do this estimation is to replicate the luminosity spectrum. The idea is to work with dN/dE_{dep} as a model-distribution of the reconstructed luminosity spectrum, use it to simulate many such spectra and locate numerically the MPV of each simulated spectrum in order to obtain a distribution of MPV-locations, with an MPV and width which represent the MPV location and its uncertainty.

In this method, unlike the previous method discussed, both sides of the luminosity spectrum peak are used to locate the MPV. Therefore a proper reconstruction of the c.m.s. energy is required, in order to avoid distortion of the reconstructed luminosity spectrum which may lead to a bias in the peak location. In order to avoid mis-reconstruction of the energy due to radiation prior to the Bhabha scattering, a back-to-back cut is introduced, requiring the

diffrence in impact angle of the two leptons to be less than 0.06 mrad (three times the angular resolution of the LumiCal in CLIC, method of calculation suggested in [12]). In order to avoid mis-reconstruction of the c.m.s. energy due to detector geometry, the fiducial volume cut was applied. The resulting spectrum of fully reconstructed events, $1/NdN_{f.r.}/dE_{dep}$, was used as model-distribution and it is shown in Fig. 3.7a.

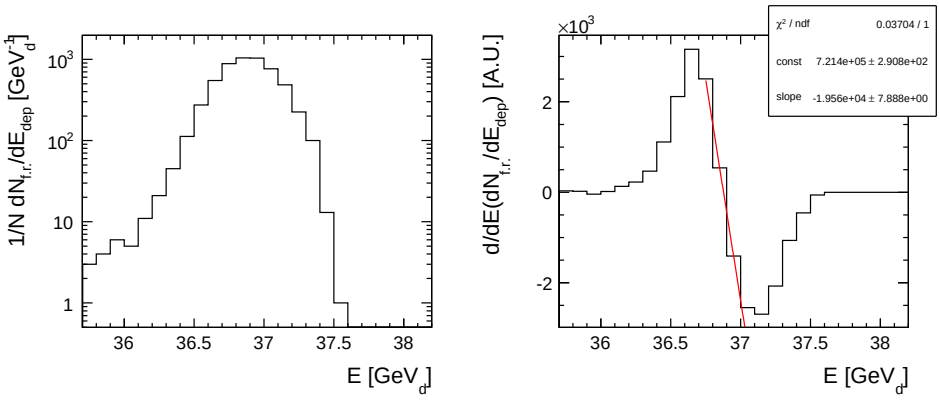

(a) (b)

Figure 3.7: (a) The reconstructed luminosity spectrum after fiducial volume and back-to-back cuts, $1/NdN_{f.r.}/dE_{dep}$. (b) A numerical derivative of the reconstructed luminosity spectrum, $d/dE(dN_{f.r.}/dE_{dep})$, with a linear fit applied around the intersection point with the energy axis.

The simulated spectra are generated from the model-distribution bin-by-bin. Every bin of the reconstructed luminosity spectrum represents a Poisson-like distribution, of the number of Bhabha scattering events produced in a certain c.m.s. energy for a fixed integrated luminosity. For each spectrum the location of the MPV, denoted here as $E_{\text{intersect}}$, is determined as follows: first, the spectrum is derived numerically. In first order approximation, the derivative may be assumed to behave linearly around the peak. Therefore a linear fit to the derivative was applied in the vicinity of the point where the derivative intersects the energy axis. Due to the fact that this method simulates many repetitions of the luminosity spectrum measurement based on the bins uncertainty, the bin-bin correlations of the spectrum which comes about from events migrating between bins (due to detector resolution smearing, for example) are taken here automatically into accout.

An example for the derivative and fit is shown in Fig. 3.7b, where

$$d/dE(dN_{f.r.}/dE_{dep})$$

is shown with a linear fit applied. The value of the intersection energy, $E_{\text{intersect}}$, from the fitted linear function is used as estimation for the MPV of the simulated spectrum. In Fig. 3.8 the normalized distribution of $E_{\text{intersect}}$ obtained from 1,600 simulated spectra is shown, overlayed with, $dN/dE_{\text{reco,3TeV}}$, the normalized reconstructed energy spectrum of 160,000 back-to-back 3 TeV e^+e^- pairs. The expectation value and RMS of the latter distribution provides a measure of the expected energy scale (normalized by 3 TeV) and its uncertainty. One evident difference between $d/dE(dN_{f.r.}/dE_{dep})$ and $dN/dE_{\text{reco,3TeV}}$ is that the latter peaks at a slightly lower energy. This difference may originate from the peak structure shown at Fig. 3.4, as it is a-symmetric around the maximum of the distribution towards $\sqrt{s'} < 1$. One more reason for this difference may be that the back-to-back cut is rather loose in this analysis. However, taking a tighter cut would have reduced statistics. The energy scale estimated in this method is equal to $3\,\text{TeV}/36.8834(66)\,\text{GeV}_\text{d}$, and its uncertainty is 0.02%. The scale is again biased, and this may be corrected for, however the contribution of the bias to the systematic uncertainty is small enough so that the measurement still meets precision requirements. The conclusion is that this method may be used for the purpose of in-situ calibration of the LumiCal, with a sufficient accuracy.

The results of this chapter are summarized in Table 3.2.

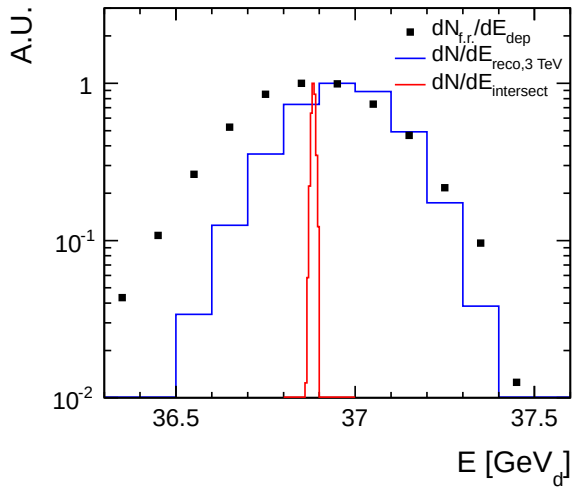

Figure 3.8: The normalized reconstructed energy spectrum of mono-energetic, back-to-back, 3 TeV e^+e^- pairs (blue line), $dN/dE_{\mathrm{reco,3TeV}}$, overlaid with the normalized distributions of $dN/dE_{\mathrm{intersect}}$ (red line) and $d/dE(dN_{f.r.}/dE_{dep})$ (black markers).

Summary of LumiCal energy measurement parameters and uncertainties				
		Prediction		Requirement
LumiCal energy resolution	E_{MPV}	18.5	GeV_d	–
		$8 \cdot 10^5$	fC	–
	σ_{reco}	0.1	GeV_d	–
		$0.04 \cdot 10^5$	fC	–
	a_{res}	0.21	$\sqrt{GeV}$	–
	fiducial volume limits	$44 < \theta < 80$	mrad	–
LumiCal energy scale	single e^-	$0.0811 \pm 2 \cdot 10^{-5}$	TeV/GeV_d	–
		$1.863 \cdot 10^{-6} \pm 5 \cdot 10^{-10}$	TeV/fC	–
	in-situ	$0.0813 \pm 16 \cdot 10^{-5}$	TeV/GeV_d	–
		$1.866 \cdot 10^{-6} \pm 4 \cdot 10^{-10}$	TeV/fC	–
	uncert. on in-situ energy scale	0.02	%	0.9%

Table 3.2: Summary of the LumiCal energy resolution and calibration results quoted in units of deposited energy, (*detector* GeV or GeV_d, as well as in units of collected charge, fC.

Chapter 4

Beam-Induced Background

4.1 Beam-Beam Effects as Background for Luminosity Measurement at the CLIC

As discussed in Section 2.1.2, beamstrahlung photons are emitted due to very strong beam-beam space charge effects. A high-energy beamstrahlung photon can turn into an electron-positron pair in the strong electromagnetic field that prevails around the beams. These so-called coherent pairs initially have small angles, and their impact as background can be reduced by adequate design of the line for the spent beam. However,iii the production of incoherent e^+e^- pairs through two photon processes can lead to signifcant background at all energies, and cannot be reduced in the same manner. Another significant background source is the interaction of real and virtual photons from the colliding beams, that can lead to multi-peripheral two-photon interactions producing hadronic final states: $\gamma\gamma \rightarrow$ hadrons [32].

When approaching the luminosity measurement, an estimation of the background signature in the LumiCal is necessary. For this purpose, the beam-beam interaction events were simulated and passed through the full detector simulation. The beam-induced backgrounds particles charachteristic features and their energy depositions in the LumiCal are presented in this chapter. Estimations of background signature are particularly relevant for readout electronics considerations and design, therefore in this chapter, energy depositions are translated to charge collected in the detector.

4.1.1 Incoherent Pairs

There are three main physical processes responsible for the production of incoherent pairs, the Bethe-Heitler (BH) process of the interaction of a real photon and a virtual photon associated with a beam particle; the Breit-Wheeler (BW) process, which is the interaction between two real photons from beamstrahlung; and the Landau-Lifshitz (LL) process of the interaction between two virtual photons. These processes are depicted in Fig. 4.1. A parametrisation of the BW, BH and LL cross sections can be found in [33].

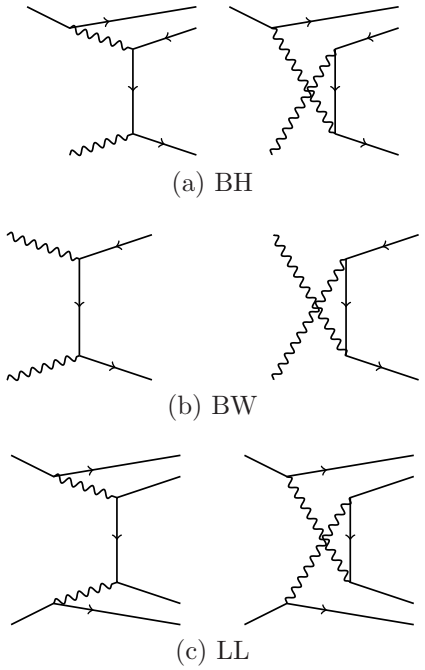

(a) BH

(b) BW

(c) LL

Figure 4.1: Feynman diagrams of the three main physical processes responsible for production of incoherent pairs; Bethe-Heitler, Breit-Wheeler and Landau-Lifshitz, as label in the figure.

Incoherent pairs can have rather large production angles with respect to the beam axis, producing a signifcant background in the detector. At a c.m.s. energy of $\sqrt{s} = 3\,\text{TeV}$and luminosity of $5.9 \cdot 10^{34}\,\text{cm}^{-2}\,\text{s}^{-1}$, the predicted number of incoherent pair particles and their total energy per BX are $3 \cdot 10^5$ and $2.3 \cdot 10^4\,\text{TeV}$, respectively [2].

4.1.2 $\gamma\gamma \rightarrow$ hadrons

In high-energy two-photon collisions, the photons can interact as point-like particles (direct contribution) or as hadron-like states (resolved contribution). The latter contribution, which leads to the concept of the photon structure function, is usually understood as originating from a fluctuation of a photon into a quark-antiquark ($q\bar{q}$) pair before interaction. These fluctuations make the photon interact strongly and are responsible for the major part of the $\gamma\gamma$ total cross section [34, 35]. Depending on the spacial configuration of the fluctuation, the $q\bar{q}$ pair may preserve its partonic nature (small size configuration) or collapse into a vector meson like state (large size configuration). In modeling interactions involving photons, the former fluctuations constitutes the anomalous contribution to the cross section and the latter to the so-called VMD contribution [32].

The $\gamma\gamma$ interactions may be divided into six classes of processes based on the photons state prior to the interaction [32], as depicted in Fig. 4.2. A photon may be found in one of the following three configurations: VMD, where the photon turns into a vector meson before the interaction; *direct*, where the "bare" photon interacts with a parton originating from the other photon; *anomalous*, where the photon perturbatively branches into a $q\bar{q}$ pair, and one of these (or a daughter parton thereof) interacts with a parton originating from the other photon.

An estimated parametrisation of the total $\gamma\gamma$ cross section, $\sigma_{\gamma\gamma}$, is given by [32],

$$\sigma_{\gamma\gamma}(s_{\gamma\gamma}) = 211\text{nb}(\frac{s_{\gamma\gamma}}{\text{GeV}^2})^{0.0808} + 215\text{nb}(\frac{s_{\gamma\gamma}}{\text{GeV}^2})^{-0.4525}, \tag{4.1}$$

where $s_{\gamma\gamma}$ is the $\gamma\gamma$ c.m.s. energy squared.

All of the hard $\gamma\gamma$ interactions can produce particles at large angles relative to the beam line [2]. At CLIC, the predicted average number of $\gamma\gamma \rightarrow$ hadrons events within the full detector acceptance at $\sqrt{s} = 3\,\text{TeV}$ is 3.2 per BX for a $\gamma\gamma$ c.m.s. energy greater than 2 GeV [2].

4.2 Background Events Sample

Both samples of background events were generated using high-energy physics simulation programs, as well as standard ILC software packages.

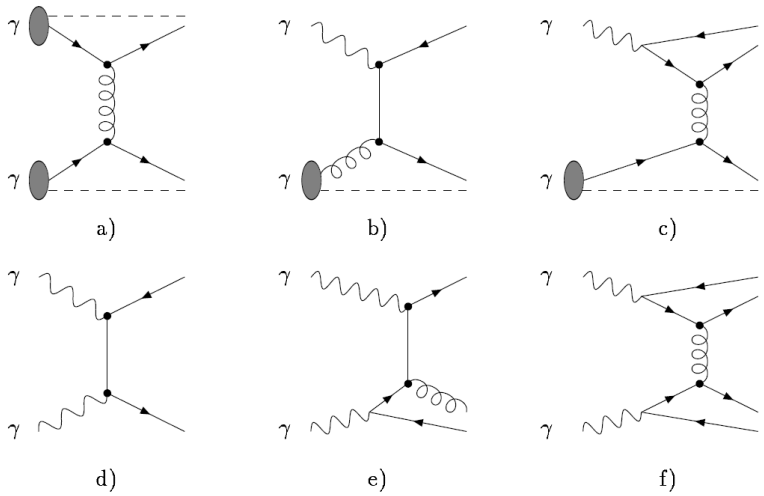

Figure 4.2: The six classes of processes contributing to hard photon-photon interactions as following: a) VMD×VMD, b) VMD×direct, c) VMD×anomalous, d) direct×direct, e) direct×anomalous, and f) anomalous×anomalous.

First, the particles produced by the beam-beam interaction (such as beamstrahlung photons) were generated using GuineaPig [18]. For the purpose of evaluating the impact of the $\gamma\gamma \rightarrow$ hadrons background in the detector, the spectrum of colliding photons from GuineaPig are used to generate events using the PYTHIA program [36]. PYTHIA simulates the interaction and the subsequent hadronisation, based on Eq. (4.1). The background particles were then passed through MOKKA [29] with the GEANT4 [30] QGSP_BERT_HP physics list. Finally, MARLIN [31] was used in order to transfer the MOKKA output into ROOT format files.

For convenience, both samples of background events were divided to BXs. This is in accordance with the time period between the readout electronics sequential samplings, that will be no less than the BX seperation time (0.5 ns). The total number of background events and the corresponding number of BXs, for both background samples, are presented in Table 4.1.

Background classification	# of simulated events	# of BX for analysis
$\gamma\gamma \rightarrow$ hadrons	63,651	19,898
incoherent pairs	1,979,393	1850

Table 4.1: The number of simulated background events, and the matching number of BX for analysis. For incoherent pairs, the number of simulated events represents the events for which a charge was deposited in the LumiCal.

The distributions of the generated background-particles properties are shown in Fig. 4.3 and Fig. 4.4. The energies of generated background particles range from $\sim 100\,\text{keV}$ to $\sim 1\,\text{TeV}$ for $\gamma\gamma \rightarrow$ hadrons; most particles have energy of about $1\,\text{GeV}$. For incoherent pairs, the energies range from a few MeV to $\sim 100\,\text{GeV}$ and most have energy of about $1 - 10\,\text{GeV}$. Above 40% of the background particles are generated with a polar angle of less than $110\,\text{mrad}$ relative to the beam-line. It is distributed assymetrically around the incoming beams for incoherent pairs, as more of the particles are generated towards the positive x direction than the negative. The RMS of the distribution is $0.041\,\text{rad}$, which means that most background particles should enter the LumiCal from the inner-most area. For $\gamma\gamma \rightarrow$ hadrons the generated polar angles are distributed symmetrically around $\theta = 0$ with a nominal RMS value of $0.54\,\text{rad}$; this means that the flux of particles hitting the detector spreads more evenly over the LumiCal geometrical volume.

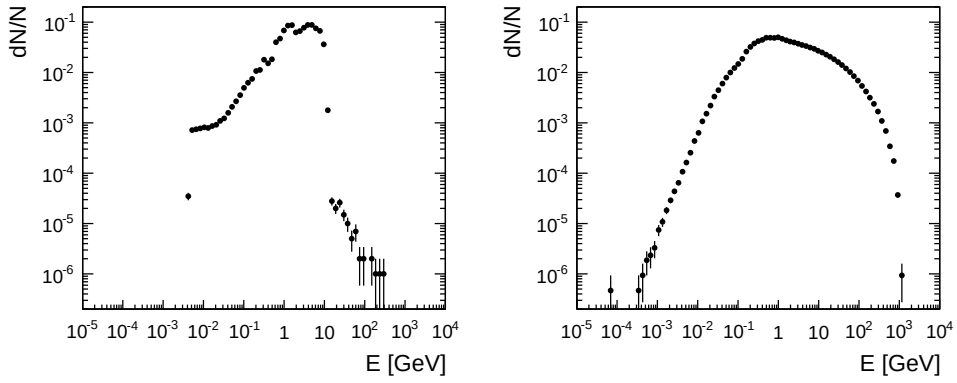

(a) (b)

Figure 4.3: The energy distribution of generated (a) incoherent pairs and (b) $\gamma\gamma \rightarrow$ hadrons particles.

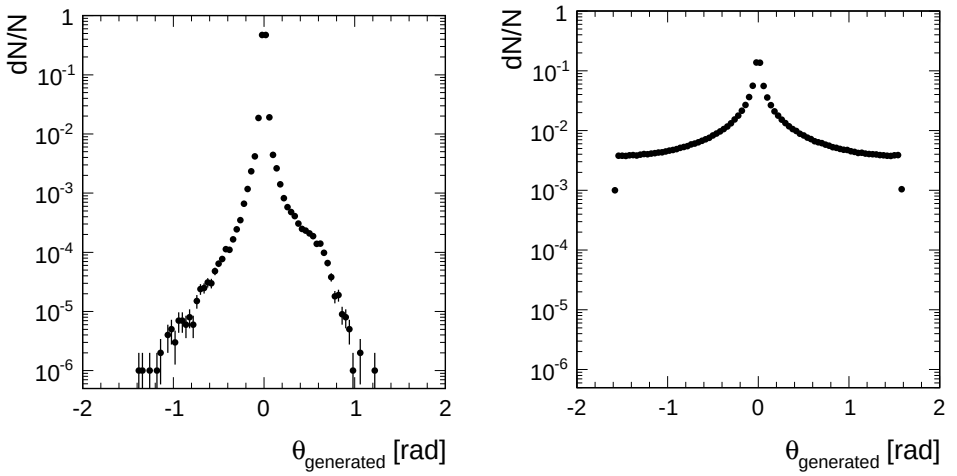

(a) (b)

Figure 4.4: Distribution of the polar angle, with respect to the incoming beams, of generated (a) incoherent pairs and (b) $\gamma\gamma \rightarrow$ hadrons particles.

4.3 Background Charge Deposits in the LumiCal

A distribution of the total background charge deposited in the LumiCal during one BX, Q_{BX}, is shown in Fig. 4.5. For incoherent pairs, this distribution peaks at $\sim 5 \cdot 10\,\text{pC}$, and may fluctuate around this value by $\sim 500\,\text{fC}$. The case is different for the $\gamma\gamma \rightarrow$ hadrons; the Q_{BX} distribution is very wide and peaks at $\sim 5 \cdot 10^5\,\text{pC}$. One implication of these fluctuations between BXs in both background types is that the LumiCal energy resolution may deteriorate, as discussed in chapter 5.

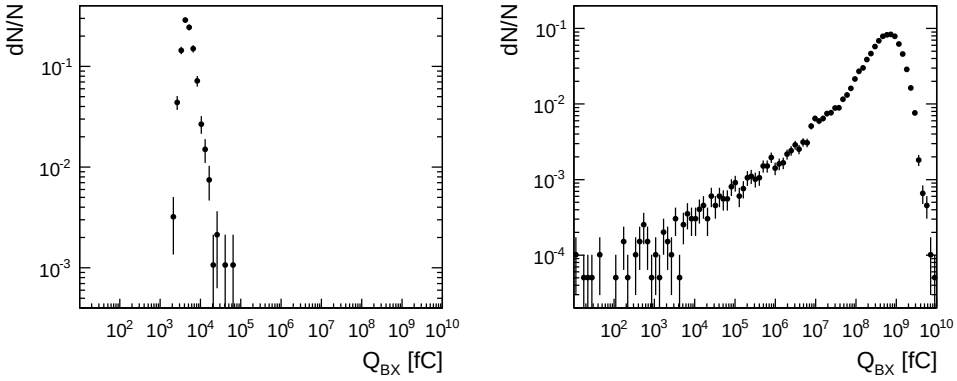

(a) (b)

Figure 4.5: Distribution of the total charge deposited per BX, Q_{BX}, in the LumiCal for (a) incoherent pairs (b) $\gamma\gamma \rightarrow$ hadrons background.

For azimuthal symmetry considerations, a numbering scheme to divide the detector to rings may be employed as follows: each ring shall be numbered by two indices, N_{layer} and N_{rad}, which stand for layer and radial segment of the sensor tiles, respectively. For the inner-most ring $N_{rad} = 0$ and for the first layer $N_{layer} = 0$.

The occupancy per BX of incoherent pairs and of $\gamma\gamma \rightarrow$ hadrons background, in the different LumiCal rings, is shown in Fig. 4.6. As in the background studies for other CLIC_ILD subdetectors [37], only those hits with a signal above 0.2 MIP (18 keV) are taken into account. The occupancy is not uniformly distributed over the volume of LumiCal. The highest occupancy for incoherent pairs occurs around the inner-most rings of the

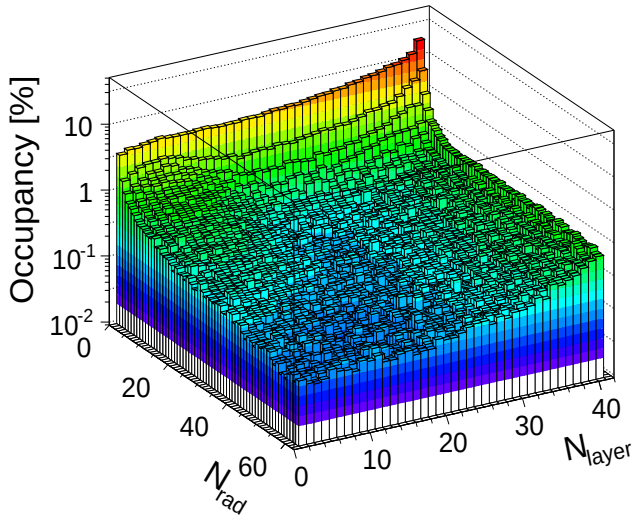

(a)

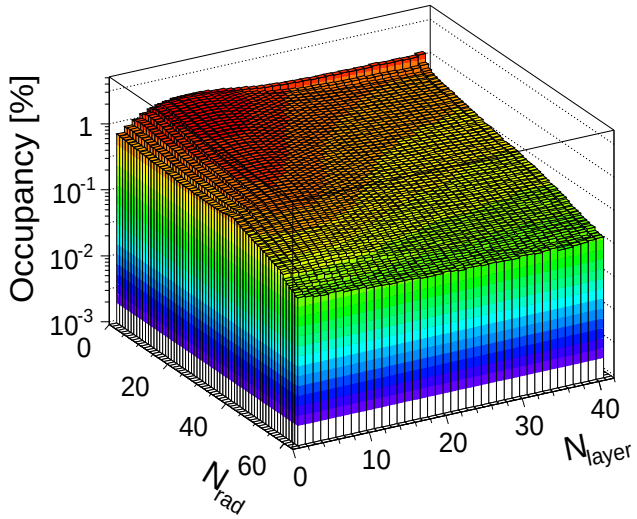

(b)

Figure 4.6: The occupancy of charge deposition above 0.2 MIP in LumiCal pads from (a) incoherent pairs and (b) $\gamma\gamma \rightarrow$ hadrons, as a function of the ring in which the pad is located, defined by N_{layer} and N_{rad}.

LumiCal, where it ranges from 3% in the front layers to 20% in the back layers. The latter is due to particles radiated at very low angles relative to the beam line and entering the LumiCal from the inner walls. For most of the calorimeter volume the occupancy is otherwise significantly below 1%. An increase in the occupancy is registered towards the back layers for high radii where it is of slightly less than 1%, due to back-scattered particles, induced by beamstrahlung remnants hitting the downstream beam-pipe and magnets. For $\gamma\gamma \rightarrow$ hadrons, the highest occupancy is in the front layers and low radii, where its value is about 1%. In the back layers and outer radii the occupancy decreases down to 0.1%.

Distribution of Q_{pad}, the charge deposited in a single LumiCal pad due to one background event, is shown in Fig. 4.7, excluding the zero charge deposits. In order to obtain the value of charge deposited in the LumiCal pads, Eq. (3.1) was used. Generally, for both background types Q_{pad} ranges from 10^{-8} to 10^{4} fC. The mean and RMS of the Q_{pad} distribution is 0.8 fC and 21.2 fC respectively for incoherent pairs; for $\gamma\gamma \rightarrow$ hadrons it is 5.3 fC and 7.8 fC, respectively. Currently, the front-end electronics design allows to study charge depositions of up to 10 pC per pad [26]. As the charge deposited per pad will be integrated over more than one event, saturation may occur.

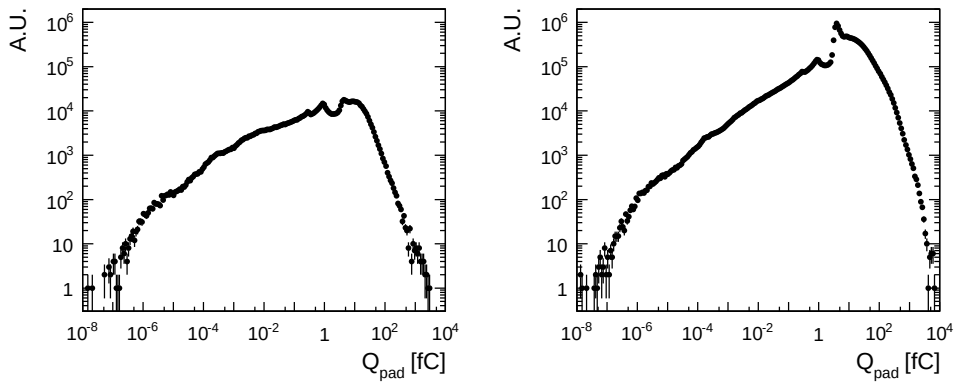

(a) (b)

Figure 4.7: The distribution of charge deposited in a single pad, Q_{pad}, by one (a) incoherent pair and (b) $\gamma\gamma \rightarrow$ hadrons background event.

The average charge deposit per pad in the different LumiCal rings in one BX, can be seen in figure Fig. 4.8. The charge deposited in a pad depends on the number of shower particles that passed through that pad. Therefore, considering that the particles may enter the detector mainly from

the front-layers and inner-most radial area, the charge deposits in this area is the highest, reaching a value of 0.75 fC and 0.86 fC for incoherent pairs and $\gamma\gamma \rightarrow$ hadrons, respectively.

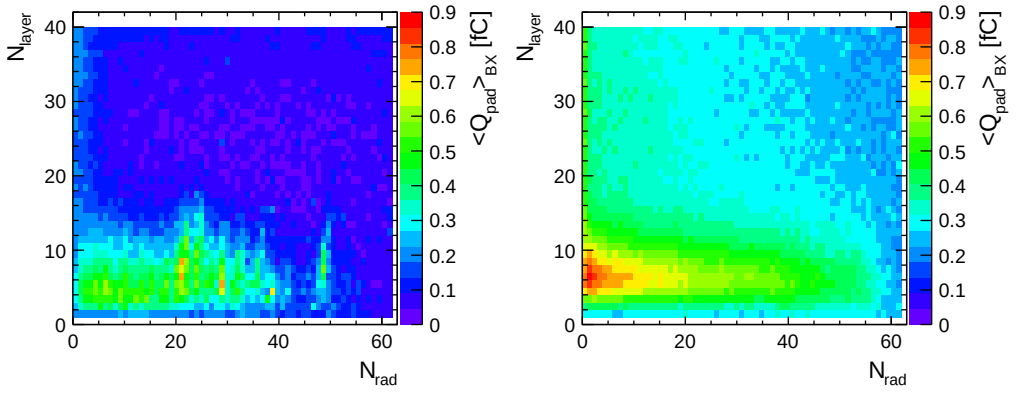

(a) (b)

Figure 4.8: The average charge deposited per BX in the LumiCal pads, by (a) incoherent pairs and (b) $\gamma\gamma \rightarrow$ hadrons background.

The relative contributions of Bhabha electrons signal and both background sources can be seen in Fig. 4.9, where the longitudinal charge deposit profile of an electron is overlayed with the expected accumulated background deposits from 20 BX (benchmark for readout sampling rate [26]). The background charge deposits are summed over those pads which lie within the envelope of a 1.5 TeV electron shower (the method for summing over relevant pads is further explained in Section 5.1). As expected considering the distributions presented in Fig. 4.8, the deposited charge demonstrates a strong dependence on the scattering angle of the Bhabha electron. The background charge deposits shown in Fig. 4.9 are averaged over electron scattering angle of $43 - 50$ mrad which is the lowest angular range of the LumiCal fiducial volume, where the background contribution is highest. In the maximum of the shower, the background may contribute up to about 2.5% of the electron contribution. In the last layers the background is nearly comparable to the signal. On average, the total charge deposited by a single electron is about 800 pC, whereas the total charge accumulated in LumiCal due to 20 BX of background is ~ 8 pC from $\gamma\gamma \rightarrow$ hadrons, and ~ 3 pC from incoherent pairs. This accumulated background charge is comparable to the expected energy resolution (~ 4.2 pC) for a 1.5 TeV electron.

The results of this chapter are summarized in Table 4.2.

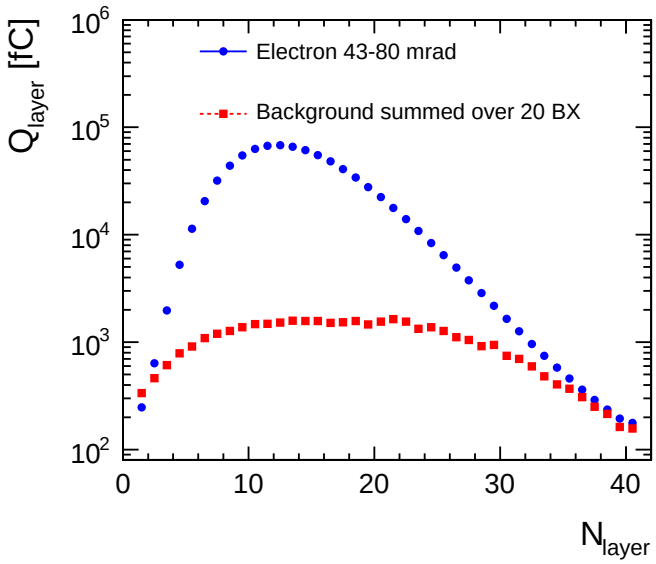

Figure 4.9: Charge deposit profile of the e^- (blue dots) as a function of the layer number in LumiCal, overlayed with background charge deposits in e^- pads (red squares), summed over 20 BX.

Summary of beam-induced backgrounds charge and energy depositions in the LumiCal				
	Incoherent-pairs	$\gamma\gamma \rightarrow$ hadrons	1.5 TeV e^-	units
Average dep. during 1 BX, full calorimeter	50	$500 \cdot 10^3$	–	pC
	1.1	$11 \cdot 10^3$	–	GeV_d
Average dep. during 20 BX, e^- pads	3	8	800	pC
	0.07	0.2	18	GeV_d

Table 4.2: Summary of the beam-induced backgrounds charge and energy depositions in the LumiCal quoted in units of charge collected, as well as in units of deposited energy.

Chapter 5

LumiCal Performance in Presence of Background

At the CLIC, unprecedent rate of background events per BX is expected. The energy deposited in the LumiCal due to background events is subject to fluctuation. The contribution of these fluctuations to the uncertainty in the energy measurement needs to be added to the contribution from the detector intrinsic fluctuations discussed in Section 3.2. This will allow an estimation of the energy measurement performance in the presence of background. The purpose of this estimation is to obtain the lower bound for the readout time stamping. Details of calculation and quantitative results are presented and discussed in the following.

5.1 Energy Resolution

The contribution of the background to the resolution will depend on the time stamping. Typically, the timing requirements for the various sub-detectors at the CLIC are of the order of 10 ns, which translates to 20 BXs. Assuming an integration over more than one BX, the energy resolution parameter with background, a_{res}^{wb}, is defined as follows:

$$\frac{a_{res}^{wb}}{\sqrt{E_b}} = \frac{\sqrt{\sigma_e^2 + N_{BX}\sigma_b^2}}{E_{mean}} \tag{5.1}$$

where E_b is the beam energy given in GeV, N_{BX} is the number of integrated BXs, σ_e and E_{mean} are the RMS and mean of the energy deposited in the

LumiCal by a 1.5 TeV electron respectively, σ_b is the RMS of the BXs energy deposit in the e^- shower pads. Relying on the fact that the average background deposits can be measured and subtracted, the value of E_{mean} is derived from the electron alone.

In previous studies, a clustering algorithm for electromagnetic shower reconstruction was developed and successfully applied for LumiCal at the ILC (see reference [12]), and it is assumed to be valid for the LumiCal at the CLIC. In this analysis, instead of the clustering algorithm, information from MC was used to extract the energy deposit under the e^- shower. For each background sample and impact angle bin, a number of 1.5 TeV electron showers that corresponds to the number of BX available were simulated in the LumiCal. The energy deposits accumulated in the LumiCal pads due to background events during one BX were summed over the full calorimeter, only for pads that registered a hit from a simulated 1.5 TeV electron shower. The distribution of this total accumulated energy deposit over all BXs was used to extract σ_b. In this manner, the fluctuations of the number of pads hit by the electromagnetic shower and the fluctuations of background events and the corresponding energy deposits in the LumiCal between the different BXs are taken into account. The average energy deposit per BX under the e^- shower, $E^{e^-}_{BX}$, is shown in Fig. 5.1 as a function of the electron impact angle, θ_{gen}, for impact angles within the fiducial volume. For $\gamma\gamma \rightarrow$ hadrons background it is 0.3 $\mathrm{GeV_d}$ at most, whereas for pairs it is 0.1 $\mathrm{GeV_d}$ at $\theta_{gen} =$ 44 mrad low impact angles and decreases by about one order of magnitude as θ_{gen} increases to $\theta_{gen} = 80$ mrad. These values are to be compared with the average energy deposited by a 1.5 TeV electron in the LumiCal, 18.48 $\mathrm{GeV_d}$ (see Section 3.2.2).

The energy resolution without and with background (a_{res} and a^{wb}_{res}, respectively) is shown in Fig. 5.2 as a function of the impact angle, for different values of N_{BX}. For convenience, the ratio of the resolution with background to the intrinsic resolution is also shown in Fig. 5.3. As expected, accumulation of background energy depositions over many BX adds fluctuations and hence deteriorates the energy resolution. Generally, the contribution of the $\gamma\gamma \rightarrow$ hadrons background to the deterioration in the energy resolution is more significant than that of the incoherent pairs background. The $\gamma\gamma \rightarrow$ hadrons background energy deposit fluctuates much more between BXs than that of the incoherent-pairs, which is also evident in Fig. 4.5 where the distribution of background energy deposit per BXs is shown. Within the fiducial volume of the LumiCal, if summed over a full train (312 BXs), the contribution of background energy deposits deteriorates the resolution by at most 24% for incoherent pairs and 544% for $\gamma\gamma \rightarrow$ hadrons. Summing over

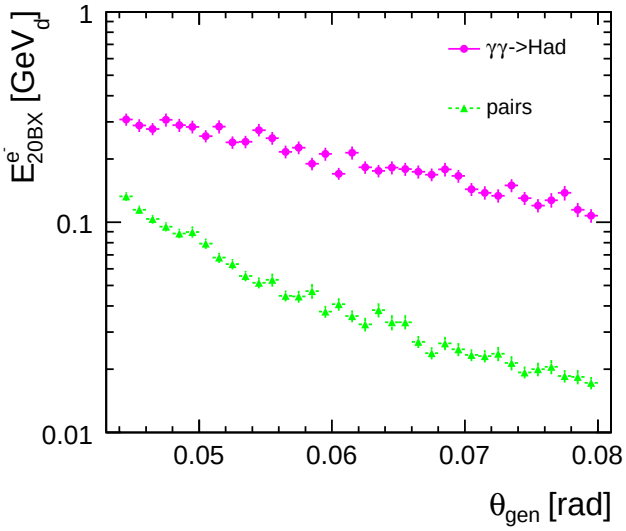

Figure 5.1: The average energy deposit under the e^- shower during 20 BX, $E^{e^-}_{20BX}$, for pairs and $\gamma\gamma \rightarrow$ hadrons background as indicated in the figure, quoted in the *detector units* $\mathrm{GeV_d}$, as a function of the electron impact angle, θ_{gen}.

20 BX may deteriorate the resolution by at most 5% and 92%, respectively.

The energy resolution in presence of both types of backgrounds, a^{cb}_{res}, is formulated similarly to Eq. (5.1),

$$\frac{a^{cb}_{res}}{\sqrt{E_b}} = \frac{\sqrt{\sigma_e^2 + N_{BX}(\sigma^2_{pairs} + \sigma^2_{\gamma\gamma})}}{E_{mean}} \tag{5.2}$$

where $\sigma_{\gamma\gamma}$ and σ_{pairs} are the measure of fluctuations in the deposited energy during one BX in the e^- pads due to $\gamma\gamma \rightarrow$ hadrons and pairs background, respectively.

Shown in Fig. 5.4 is a^{cb}_{res} as a function of the e^- impact angle, θ_{gen}, for background integration over different number of BXs, as denoted in the figure. The resulting energy resolution in presence of incoherent pairs- and $\gamma\gamma \rightarrow$ hadrons combined backgrounds is deteriorated by at most 548% if summed over a full train, and by at most 93% if summed over 20 BXs.

The conclusion of this study is that the background fluctuations, assuming a time stamping of 20 BX, may increase the resolution by as much as about

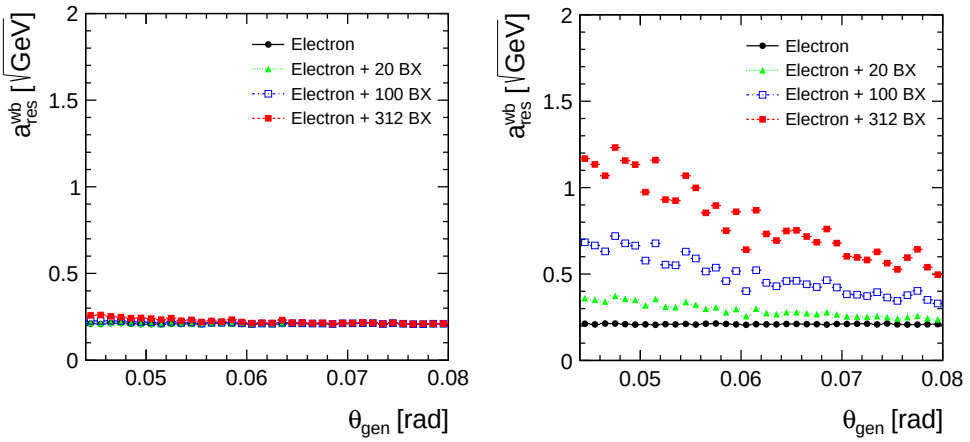

Figure 5.2: Measure of a_{res}^{wb}, the energy resolution in presence of (a) incoherent pairs (b) $\gamma\gamma \rightarrow$ hadrons background, as a function of the e^- impact angle, θ_{gen}. The background is integrated over different number of BXs, as noted in the figure. Also shown is the intrinsic resolution, a_{res}, obtained in the absence of background.

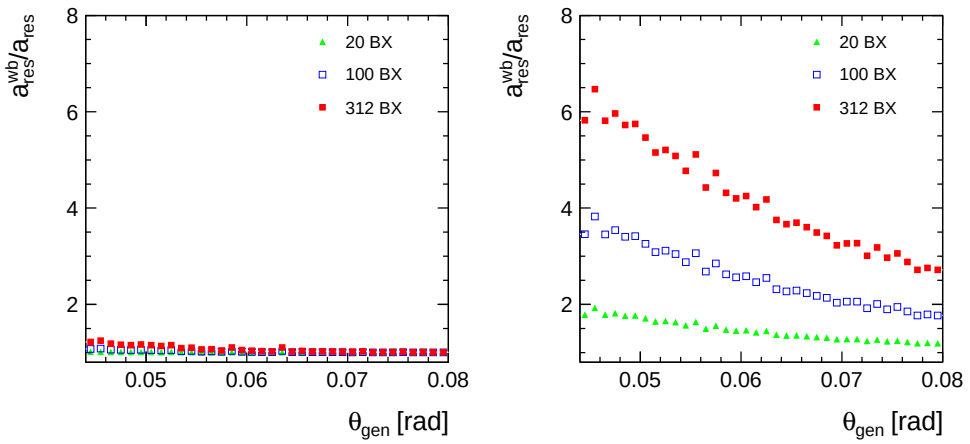

Figure 5.3: Measure of the ratio between the energy resolution with and without background, a^{wb}_{res} and a_{res} respectively, as a function of the e^- impact angle, θ_{gen}, for (a) incoherent pairs (b) $\gamma\gamma \rightarrow$ hadrons background. The background is integrated over different number of BXs, as denoted in the figure.

10%. This means that the time stamping of the readout system should be as frequent as possible, within reasonable resources consumption. A good time resolution is the key to control the uncertainty in energy and hence in luminosity measurement.

The results of this chapter are summarized in Table 5.1.

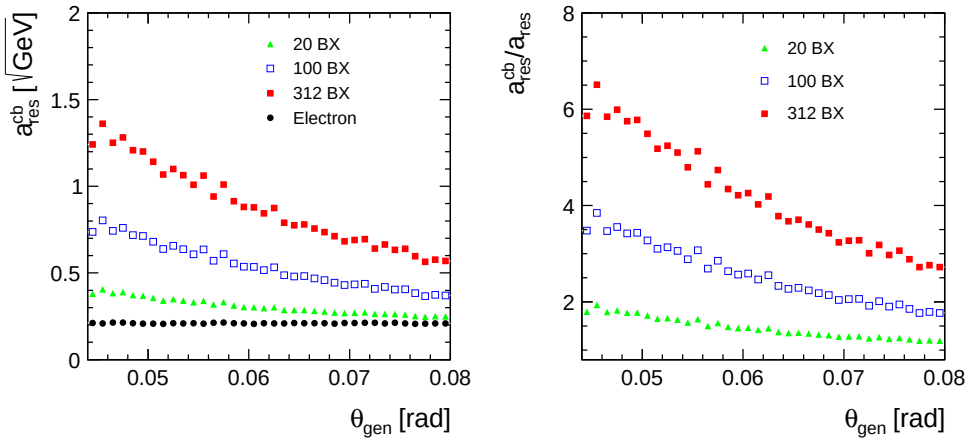

(a) (b)

Figure 5.4: Measure of (a) the energy resolution in presence of both backgrounds, a^{cb}_{res} (see Eq. (5.2)) (b) measure of the ratio between the energy resolution with and without both backgrounds a^{cb}_{res} and a_{res} respectively, as a function of the e^- impact angle, θ_{gen}, for background integration over different number of BXs, as denoted in the figure.

Summary of a_{res}^{wb} in presence of beam-induced background			
	Incoherent-pairs	$\gamma\gamma \rightarrow$ hadrons	both bg. combined
a_{res}^{wb}/a_{res}, intg. over 20 BX	105%	192%	193%
a_{res}^{wb}/a_{res}, intg. over 312 BX	124%	644%	648%

Table 5.1: Summary of the energy resolution coefficient, a_{res}^{wb}, nominal values in presence of beam-induced backgrounds.

Summary

The compact linear collider is a proposed multi-TeV e^+e^- linear collider, with excellent prospects to complement and to extend the Large Hadron Collider physics program, both in discovery potential and in the ability to provide high precision measurements. The information obtained from the CLIC may also provide the ability to discriminate between models of new physics and their fundamental parameters. In order to match the expected statistical error for measuring cross sections of most electroweak processes in a typical year ($500\,\mathrm{fb}^{-1}$) the integrated luminosity of the CLIC will have to be known with a precision of 10^{-2}, which poses a significant challenge. Luminosity at the CLIC is measured by counting Bhabha scattering events, reconstructed in the luminosity calorimeter. LumiCal, a precision tungsten-silicon calorimeter, will provide a measurement of the integrated luminosity. Positioned at low angles, it is exposed to significant amount of beam-induced background, which affects its performance.

For the first time, the issue of in-situ calibration of the LumiCal is addressed. It has been shown here that it is possible to use the luminosity spectrum peak-area, as reconstructed from the LumiCal, in order to measure the LumiCal energy scale factor with an estimated accuracy of 0.02%, lower than accuracy of 0.9% derived from the requirement on the luminosity measurement. The energy scale predicted is $0.081 \pm 16 \cdot 10^{-5}\,\mathrm{TeV/GeV_d}$.

In addition, a study has been presented in which the implications of beam-induced background on the LumiCal energy resolution are quantified. Integration of the LumiCal readout system output signal over time will enhance the effect of background charge deposits fluctuations. Consequently, a deterioration is foreseen in the LumiCal performance. The energy resolution in presence of incoherent pairs- and $\gamma\gamma \rightarrow$ hadrons combined backgrounds compared to the intrinsic energy resolution, 0.21 GeV, is deteriorated by at most 548% if summed over a full train, and by at most 93% if summed over 20 BXs.

Acknowledgments

First, I thank my supervisors, Prof. Halina Abramowicz and Prof. Emeritus Aharon Levy, for introducing me to the world of particle physics, for your time and efforts, for expecting and encouraging high achievements, and for your most-valuable guidance and personnal support throughout challenging periods.

I would like to thank the members of my research group; Orel Guetta, Dr. Ronen Ingbir, Dr. Sergey Kannanov, Iftach Sadeh, and Amir Stern, your help, advices and company are highly appreciated. It was a great privilege to work with all of you. I would also like to thank Oron Rosenblat and Reuven Balkin, for your help in the past months. A special gratitude is dedicated to Itamar Levy, for advices and discussions about experimental and theoretical physics, for the time shared together during research, courses and breaks, and for your generosity, support and friendship. My gratitude is also dedicated to all friends and collegues from the HEP lab at the Tel-Aviv University, in particular to Dr. Yan Benhammou, Mr. Menny Ben-Moshe and Mr. Yonathan Monbaz, for your encouragement, care and proffesional support, and for cheerful time spent together at coffee breaks and beyond.

I wish to deeply thank all friends and collegues from the FCAL collaboration. I would like to express a special appreciation to Dr. Wolfgang Lange and Prof. Wolfgang Lohman for your proffesional guidance and for your hospitality at DESY Zeuthen, and to Mr. Andre Sailer for help in coping with the ILC software tools.

To all my friends and family, thank you for the support during this work. In particular, I would like to thank Yaron Karmi, Adiel Meyer and Shiri weinstein for their special efforts and help. And finally, my deep gratitude is dedicated to Genya, Yakov, Meron and Tamir, my dear family, for your endless support and encouragement.

This work was partially supported by the Israeli Science Foundation.

Bibliography

[1] H. Murayama and M. E. Peskin, *Physics opportunities of e+ e- linear colliders*, Ann.Rev.Nucl.Part.Sci. **46** (1996) 533–608, arXiv:hep-ex/9606003 [hep-ex].

[2] L. Linssen, A. Miyamoto, M. Stanitzki, and H. Weerts, *Physics and Detectors at CLIC: CLIC Conceptual Design Report*, arXiv:1202.5940 [physics.ins-det].

[3] CMS Collaboration Collaboration, F. Fabozzi, *Results on the search for the standard model Higgs boson at CMS*, AIP Conf.Proc. **1492** (2012) 10–17.

[4] ATLAS Collaboration Collaboration, R. Tafirout, *Standard Model Higgs boson searches in p p collisions at s**(1/2) = 7-TeV with the ATLAS detector*, J.Phys.Conf.Ser. **389** (2012) 012001.

[5] F. Richard, J. Schneider, D. Trines, and A. Wagner, *TESLA: The superconducting electron positron linear collider with an integrated X-ray laser laboratory. Technical design report. Pt. 1: Executive summary*, (2001) , arXiv:hep-ph/0106314 [hep-ph].

[6] *Zeroth order design report for the Next Linear Collider: Volume 1.* Stanford, Calif. : SLAC, 1996.

[7] *GLC Project: Linear Collider for TeV Physics.* KEK report. High Energy Accelerator Research Organization, KEK, Tsukuba, Japan, 2003.

[8] ILC Collaboration Collaboration, E. Brau, James et al., *ILC Reference Design Report: ILC Global Design Effort and World Wide Study*, arXiv:0712.1950 [physics.acc-ph].

[9] T. I. C. Group, *The International Large Detector: Letter of Intent*, arXiv:1006.3396 [hep-ex].

[10] H. Abramowicz et al., *Forward Instrumentation for ILC Detectors*, JINST **5** (2010) P12002, arXiv:1009.2433 [physics.ins-det].

[11] H. Abramowicz et al., *A luminosity calorimeter for CLIC*, Tech. Rep. LCD-Note-2009-02, 2009. CERN LCD.

[12] I. Sadeh, *Luminosity Measurement at the International Linear Collider*, M.Sc. thesis, Tel Aviv University, Israel, 2010.

[13] A. Guido, K. Ronald, and V. Claudio, *Z physics at LEP: proceedings*, pp. 173–194. CERN, European Organization for Nuclear Research, Geneva, 1989.

[14] W. Kilian, T. Ohl, and J. Reuter, *WHIZARD: Simulating Multi-Particle Processes at LHC and ILC*, Eur.Phys.J. **C71** (2011) 1742, arXiv:0708.4233 [hep-ph].

[15] F. Halzen and A. D. Martin, *Quarks And Leptons: An Introductory Course In Modern Particle Physics*. New York, Usa: Wiley, 1984.

[16] S. Hansen, *Measurement of Electroweak Effects in Small Angle Bhabha Scattering with the DELPHI Detector at LEP*, M.Sc. thesis, Oslo U., 1996.

[17] C. Carloni Calame, H. Czyz, J. Gluza, M. Gunia, G. Montagna, et al., *NNLO massive corrections to Bhabha scattering and theoretical precision of BabaYaga@NLO*, arXiv:1112.2851 [hep-ph].

[18] D. Schulte, *Study of electromagnetic and hadronic background in the interaction region of the TESLA Collider*. PhD thesis, 1997. DESY-TESLA-97-08.

[19] M. Frary and D. Miller, *Monitoring the luminosity spectrum*, in e^+e^- *collisions at 500 GeV*, DESY 92-123A, pp. 379–391. 1991.

[20] C. Rimbault, *Impact of Beam-beam Effects on Precision Luminosity Measurements at the ILC: Main results*, eConf **C0705302** (2007) MDI17.

[21] C. Fabjan and F. Gianotti, *Calorimetry for particle physics*, Rev.Mod.Phys. **75** (2003) 1243–1286.

[22] Particle Data Group Collaboration, K. Nakamura et al., *Review of particle physics*, J.Phys.G **G37** (2010) 075021. http://pdg.lbl.gov.

[23] I. Levy, *Detector development for the instruments in the forward region of future linear colliders*, M.Sc. thesis, Tel Aviv University, Israel, 2012.

[24] S. Kulis, *Test beam studies of the LumiCal prototype*, . EUDET-Memo-2010-09.

[25] O. Novgorodova, *Forward Calorimeters For The Future Electron-Positron Linear Collider Detectors*, . PoS **QFTHEP2010** (2010) 30.

[26] S. Kulis and M. Idzik, *Study of readout architectures for trigerless high event rate detectors at CLIC*, Tech. Rep. LCD-Note-2011-015, 2011. CERN LCD.

[27] S. Jadach, W. Placzek, and B. F. L. Ward, *BHWIDE 1.00: O(alpha) YFS exponentiated Monte Carlo for Bhabha scattering at wide angles for LEP1/SLC and LEP2*, Phys. Lett. **B390** (1997) 298–308. http://arxiv.org/pdf/hep-ph/9608412. Version 1.04.

[28] A. Stahl, *Luminosity measurement via Bhabha scattering: Precision requirements for the luminosity calorimeter*, (2005) LC-DET-2005-004.

[29] T. Behnke and F. Gaede, *Software for the International Linear Collider: Simulation and reconstruction frameworks*, Pramana **69** (2007) 1089–1092.

[30] J. Allison *et al.*, *GEANT4 Developments and Applications*, IEEE Transactions on Nuclear Science **53, No. 1** (Feb., 2006) 270–278. version 09-03 patch 02.

[31] F. Gaede, *Marlin and LCCD: Software tools for the ILC*, Nucl.Instrum.Meth. **A559** (2006) 177–180. http://ilcsoft.desy.de/portal/software_packages/marlin/index_eng.html. Version 01-00.

[32] G. A. Schuler and T. Sjostrand, *A Scenario for high-energy gamma gamma interactions*, Z.Phys. **C73** (1997) 677–688, arXiv:hep-ph/9605240 [hep-ph].

[33] K. Yokoya and P. Chen, *Beam-beam phenomena in linear colliders*, Lect. Notes Phys. **400** (1992) 415.

[34] M. Drees and R. M. Godbole, *Resolved photon processes*, Pramana **41** (1993) 83–123, arXiv:hep-ph/9302256 [hep-ph].

[35] R. Godbole, A. De Roeck, A. Grau, and G. Pancheri, *Hadronic cross-sections in two photon processes at a future linear collider*, JHEP **0306** (2003) 061, arXiv:hep-ph/0305071 [hep-ph].

[36] T. Sjostrand, S. Mrenna, and P. Z. Skands, *A Brief Introduction to PYTHIA 8.1*, Comput.Phys.Commun. **178** (2008) 852–867, arXiv:0710.3820 [hep-ph].

[37] FCAL Collaboration, D. Dannheim and A. Sailer, *Beam-Induced Backgrounds in the CLIC Detectors*, LCD-Note-2011-021, 2011.